Jingwei Xie[1,2], Hailong Liu[1,2,3*], and Pengfei Lin[1,2]

[1]LASG, Institute of Atmospheric Physics, Chinese Academy of Sciences, Beijing 100029, China

[2]College of Earth and Planetary Sciences, University of Chinese Academy of Sciences, Beijing 100049, China

[3]Center for Ocean Mega-Science, Chinese Academy of Sciences, Qingdao 266071, China

Corresponding author: Hailong Liu (lhl@lasg.iap.ac.cn)

Key Points:

- A Reynolds and coarse-graining hybrid eddy transport diagnostic framework was developed to distinguish the transient and stationary eddies
- The anisotropic transport tensor and all the tensor-related quantities are analyzed in the Southern Ocean
- The tensor's stationary component can be affected by large-scale topography, nonconservative processes, and large-scale flow structure

Abstract

Mesoscale ocean eddies dramatically impact oceanic material transport, momentum and energy budgets, and large-scale ocean circulation; therefore, reasonably diagnosing their effects is crucial for providing insights into eddy parameterization scheme development. In this work, a Reynolds and coarse-graining hybrid eddy transport diagnostic framework is proposed and applied in the Southern Ocean. Both the isotropic transport coefficient and anisotropic transport tensor are diagnosed and decomposed into contributions from transient and stationary eddies. The tensor can be split into its symmetric and antisymmetric parts, and the symmetric tensor is further diagonalized to analyze the eigenvalues and eigenvectors. We verify that the anisotropic assumption better fits the ocean mesoscale eddy transport process than the isotropic assumption, at least in the Southern Ocean. We place particular emphasis on the transport tensor's stationary component affected by large-scale topographies, nonconservative processes, and large-scale flow structures and find that its influence is highly anisotropic horizontally and varies vertically. We probe all tensor-related elements that emerge in our hybrid framework, especially the eigenvalues and eigenvectors of the symmetric tensor. We reveal all three configurations of the major and minor eigenvalues that appear in the Southern Ocean, where the one representing vortex filamentation is the most common scenario. In addition, we discover a high randomness of the eigenvectors, which implies the possibility of a semideterministic and semistochastic anisotropic parameterization scheme.

Plain Language Summary

The "flux-gradient" relationship, which links the eddy fluxes with the large-scale background gradient fields through either a scalar transport coefficient or

a transport tensor, is widely leveraged in mesoscale ocean eddy parameterization. The scalar coefficient and the transport tensor represent the isotropic and anisotropic assumptions, respectively. To use the "flux-gradient" relationship in diagnostics, one needs to carry out scale separation between eddying motion and large-scale motion. Most studies do this through zonal or temporal averaging, although such averaging would lead to a loss of local information. In this study, we apply either a spatial coarse-graining method or a 2D spatial filter to define the mesoscale eddying structure as the deviation from the filtered large-scale field. Then, the Reynolds' temporal average is used to divide the eddy effect into transient and stationary parts. In this way, we can diagnose how stationary and transient eddies contribute to the tracer transport process and provide insights into mesoscale eddy parameterization design.

1 Introduction

Ocean physical processes with a horizontal spatial scale of approximately 50-500 km or near the first baroclinic Rossby deformation radius are usually called ocean mesoscale motions; these include mesoscale eddies and meander structures. Mesoscale motions impact ocean material transport, momentum budget, and large-scale ocean circulation and contain more than 90% of the ocean kinetic energy. Therefore, it is necessary to resolve the oceanic mesoscale process in a numerical model. However, due to the current limitations of computing power and high costs, the global climate system model that needs long-term integration cannot reach the resolution to resolve mesoscale processes. Designing a reasonable parameterization scheme for this scale is still of great interest for developing climate ocean models. For convenience, "mesoscale eddy" is used below to represent all ocean mesoscale processes and structures.

Gent and McWilliams (1990) and Gent et al. (1995) proposed a mesoscale eddy parameterization scheme to mimic the process of releasing the available potential energy (APE) by baroclinic instability for application in a noneddy-resolving ocean model (called GM parameterization). This scheme is widely practiced in climate models and has been continuously developed over the previous three decades (Treguier et al., 1997; Visbeck et al., 1997; Griffies, 1998; Griffies et al., 1998; Marshall et al., 1999; Smith & Gent, 2004; Marshall et al., 2012; Mak et al., 2017; Bachman, 2019). In essence, mesoscale eddy parameterization is a turbulent closure problem. That is, the resolved scale quantities are used to describe the overall effect of the unresolved or incompletely resolved mesoscale eddy transport process for the evolution of large-scale tracer fields (Vallis, 2017). In practice, the "flux-gradient" relationship is often applied; namely, the eddy tracer flux and the local large-scale tracer gradient field are associated by the eddy transport coefficient ( ) or the transport tensor ($\mathbf{K}$) (Nikurashin & Ferrari, 2010; Vallis, 2017).

Diagnosing the eddy transport coefficient and the transport tensor and identifying the factors that might determine them have become important topics in mesoscale eddy parameterization development. In addition to using observation data for estimation, the diagnosis of the mesoscale eddy transport effect

can also leverage high-resolution model data and separate information from different scales to estimate the integral effect of smaller scales on the large-scale background field. In the "flux-gradient" relationship, this collective effect is expressed in the eddy transport coefficient ( ) or the eddy transport tensor ($\mathbf{K}$).

A key difference between the eddy transport coefficient ( ) and the eddy transport tensor ($\mathbf{K}$) is that is based on the assumption of isotropic eddy diffusion, while $\mathbf{K}$ assumes anisotropic eddy transport. Furthermore, the symmetrical part (S) of $\mathbf{K}$ can be used to express anisotropic eddy diffusion, and the isotropic case is a specific scenario in which the eigenvalues of S are equal (see section 2.1 of this paper or Fox-Kemper et al., 2013 for details). Currently, most studies on eddy transport diagnosis and parameterization have adopted isotropic hypotheses and probed scalar eddy transport coefficients (Gent & McWilliams, 1990; Gent et al., 1995; Treguier et al., 1997; Visbeck et al., 1997; Treguier, 1999; Wilson & Williams, 2004, 2006; Zhao & Vallis, 2008; Nikurashin & Ferrari, 2010; Garabato et al., 2011; Abernathey et al., 2013). However, due to the effect, the transport caused by mesoscale eddies is stronger in the zonal direction than in the meridional direction. Therefore, the form of an anisotropic mesoscale eddy parameterization is more aligned with real-world geophysical fluid dynamics (Smith & Gent, 2004).

Recently, some studies have used the anisotropic form to diagnose the eddy transport process and found that the anisotropic result is more appropriate than the isotropic result. Abernathey et al. (2013) ran a channel model with a sponge lateral boundary layer to mimic the dynamics in the Southern Ocean and capture its stratification structure. They then diagnosed the anisotropic tensor and compared it to various isotropic scalar coefficients. Bachman and Fox-Kemper (2013), Bachman et al. (2015), and Bachman et al. (2020) developed the multi-tracer inversion technique to diagnose the eddy transport tensor through ideal numerical simulations and a high-resolution global model. Lu et al. (2016) studied both the scalar coefficients and the transport tensors in the Southern Ocean with eddy-permitting data and further decomposed the eddy effect into stationary and transient parts. Haigh et al. (2020), Haigh et al. (2021a), and Haigh et al. (2021b) made a detailed diagnosis of the anisotropic transport tensor, including its symmetric and antisymmetric parts, with a double-gyre ideal model output. Stanley et al. (2020) tried to reconstruct the vertical structure of the transport tensor $\mathbf{K}$ through vertical modes and their linear combinations. They found that the anisotropic framework could obtain much more precise vertical structure results than the isotropic framework.

Whether isotropic or anisotropic forms are adopted, the eddy transport effect can be decomposed into an advective part and a diffusive part (Lee et al., 1997; Treguier, 1999). Griffies (1998) conducted a theoretical derivation and connected the symmetric part (S) of the transport tensor ($\mathbf{K}$) to the diffusion process and the antisymmetric part (A) with either the advection process or skew flux along large-scale tracer contours. S can be further diagonalized, where its different eigenvalues represent the eddy diffusive intensities along the direction

of the corresponding eigenvector (Smith & Gent, 2004; Bachman & Fox-Kemper, 2013; Fox-Kemper et al., 2013; Bachman et al., 2015). However, due to its complexity and abstraction, the characteristics of the transport tensor are far from clear.

For the relationship between the diffusive part and the advective part, Dukowicz and Smith (1997) used the random walk model to deduce that the same diffusion tensor can be used to specify eddy diffusion and eddy-induced advection along the isopycnal surface. Smith and Gent (2004) suggested that, from the perspective of increasing convenience and reducing computation, the off-diagonal elements of the symmetric and antisymmetric parts should take the same absolute value. However, Treguier (1999) proposed that the transport coefficients of the two processes do not need to be the same when the isotropic assumption is adopted. Bachman et al. (2020) give the difference between the two processes and note that the result of Dukowicz and Smith (1997) is attributed to their failure to consider the vertical distribution of the transport tensor. In addition, Haigh et al. (2020), Haigh et al. (2021a), and Haigh et al. (2021b) followed the practice of Lu et al. (2016) to diagnose the transport tensor on isopycnal surfaces, simplified the problem into two dimensions and diagnosed a spatiotemporally varying 2×2 tensor. They found that the off-diagonal elements of S contribute significantly to the polarity of the eigenvalues (i.e., the signs of the two eigenvalues are different), while the distributions and roles of A and S are not consistent. From the above descriptions, for the complete diagnosis of K, one should consider all elements of A and S and the eigenvalues and eigenvectors of S. This precisely describes one of the strategies we adopt in this study.

In relevant works on diagnosing mesoscale eddy transport, the definitions of mesoscale eddies and their separation on a large scale are still vague. In most cases, mesoscale eddies are defined as anomalies from zonal or temporal averages, but this approach does not guarantee robust scale separation between the mesoscale and large spatial scales (Buzzicotti et al., 2021). Recently, some studies began to use either the coarse-graining method or a two-dimensional spatial filter to separate mesoscale motion from large-scale background fields (Lu et al., 2016; Aluie et al., 2018; Bachman et al., 2020; Haigh et al., 2020; Buzzicotti et al., 2021; Haigh et al., 2021a, 2021b), which is more intuitively similar to the practice of low-resolution ocean models. In particular, Lu et al. (2016) adopted a modified Lorenz-type spatiotemporal decomposition method (Lorenz, 1967), in which a two-dimensional moving box filter is used for spatial scale separation and the annual average is used for the time average. Their method is essentially a hybrid version of the Reynolds average in time and the coarse-graining method in space. We will also follow and develop their approach in this paper.

Meanwhile, this hybrid method can be used to decompose the mesoscale eddy transport tensor into the contribution of stationary eddies (SEs) and transient eddies (TEs). In terms of the mechanism, the understanding of TEs is more in-depth; namely, eddies are mainly formed when the APE is converted into kinetic energy through baroclinic instability. Therefore, the GM scheme is aimed

at TE. For the SE transport effect, it is generally believed that topographic forcing is the major contributor. Treguier and McWilliams (1990), MacCready and Rhines (2001), Garabato et al. (2011), Thompson and Sallee (2012), Abernathey and Cessi (2014), and so on found that stationary structures appear downstream of large-scale topographies and make a crucial contribution to the cross-front eddy mass and tracer transport. Abernathey and Cessi (2014) discovered that time-averaged stationary waves have the characteristics of standing Rossby waves. Youngs et al. (2017) verified that the topography could produce zonal inhomogeneity of flow and form stationary meanders downstream. They also found that both baroclinic instability and barotropic instability could play vital roles in meander dynamics. Other studies, such as Bischoff and Thompson (2014), Radko and Kamenkovich (2017), and Khani et al. (2019), leverage ideal numerical simulations to clarify the relationship between stationary phenomena and topographies. Most relevant to our study, Lu et al. (2016) showed that SEs could play a nonnegligible role in eddy transport flux and the transport coefficient or tensor in the Southern Ocean so that their effect should be involved in mesoscale eddy parameterization. Therefore, although the framework of this paper can be used to compare the contributions of TEs and SEs simultaneously, we will focus more on the results related to the stationary part and shed some light on the potential impacts of the topography on the eddy transport tensor and coefficient.

To better understand the characteristics of the mesoscale eddy transport process, this paper will first further develop the approach of Lu et al. (2016) into a Reynolds and coarse-graining hybrid eddy transport diagnostic method. The coarse-graining method is for spatial scale separation, and the Reynolds' average is for temporal separation. This hybrid framework allows us to decompose the transport tensor into stationary and transient contributions, representing the major difference from Bachman et al. (2020) and Haigh et al. (2020). This is also an anisotropic transport tensor diagnosis framework in which symmetric and antisymmetric decomposition of the tensor is performed. Unlike Lu et al. (2016), which analyzed only the diagonal elements of the transport tensor, this paper performs a complete diagnosis of all relevant elements of the transport tensor, including the four elements of the original tensor, the off-diagonal elements of both S and A and the eigenvalues and eigenvectors of S. We will demonstrate the rationality of the anisotropic assumption in the ocean mesoscale eddy transport process from several angles and focus on the contribution of SEs to the transport of potential vorticity (PV) under the hybrid framework. In addition, we will use this framework to explore the potential impact of topography on the eddy transport tensor, especially the different effects on stationary and transient transport tensors and coefficients. Upon comparison to the previous work of Lu et al. (2016), we also select the Southern Ocean as the research area. An in-depth analysis and understanding of the transport tensor will help us to comprehend the physical mechanism of the mesoscale transport process and propose a more physically complete parameterization scheme.

The outline of this paper is as follows. Section 2 introduces the diagnostic

methods, including the transient and stationary flux-gradient relationship under the hybrid framework, the anisotropic transport tensor, and further processing. In section 3, we show the diagnosis results in the Southern Ocean area and explore the influences of the topography on the transport tensor and coefficient. Section 4 is the summary and discussion.

2 Method

2.1 The "flux-gradient" relationship

Because the ocean interior satisfies the quasi-adiabatic condition, mesoscale motion occurs along isopycnal surfaces (or neutral surfaces) (McDougall, 1987; Fox-Kemper et al., 2013). Therefore, the problem can be simplified into two dimensions in density coordinates. In the average or large-scale tracer equation, there are often unresolved eddy flux divergence terms that need to be parameterized. It is assumed that the spatial scale separation of motion is established, and the mixing-length assumption is also made (Taylor, 1922; Vallis, 2017; Bachman et al., 2020); that is, if a fluid parcel deviates from its equilibrium position, its properties do not change significantly within the mixing-length distance. Then, it is not difficult to obtain the isopycnal flux-gradient relationship as

(1)

where can be any tracer field, "-" represents an averaged or large-scale quantity, " "' represents the subgrid scale quantity or deviation from the mean, and is a second-order tensor, namely,

(2)

where . This tensor can be regarded as the covariance matrix of eddy velocity and eddy displacement (or mixing length), which we call the transport tensor in this paper. This tensor is kinematic, depending on the turbulent flow state (Dukowicz & Smith, 1997; Treguier, 1999; Smith & Gent, 2004; Abernathey et al., 2013).

The transport tensor is not necessarily symmetric, and it can be further decomposed into a symmetric and an antisymmetric tensor,

(3)

(4)

(5)

The antisymmetric part (3) represents the advective transport along large-scale tracer contours, corresponding to the GM parameterization scheme (Gent & McWilliams, 1990; Gent et al., 1995; Griffies, 1998). The symmetric part (4) represents a diffusion-like effect, corresponding to the Redi diffusion parameterization scheme (Redi, 1982; Griffies, 1998). The decomposed "flux-gradient" relationship can be written as (5).

Furthermore, the symmetric tensor is diagonalized to obtain the diagonal matrix consisting of the eigenvalues and the corresponding eigenvector matrix

(6)

(7)

Here, is the major eigenvalue and is the minor eigenvalue, and they represent the diffusion strength along the major axis (parallel to the major eigenvector) and the minor axis (parallel to the minor eigenvector), respectively. represents anisotropic diffusion, and represents isotropic diffusion, in which case we can use a scalar transport coefficient to express the "flux-gradient" relationship,

(8)

Note that the eigenvalues are not necessarily positive in diagnosis (Lu et al., 2016; Bachman et al., 2020; Haigh et al., 2020; Stanley et al., 2020). When the eigenvalue is positive, positive diffusion in the corresponding axis reduces the eddy tracer variance. Anti-diffusion enhances the corresponding eddy tracer variance when the eigenvalue is negative.

2.2 Reynolds and coarse-graining hybrid decomposition

This section will introduce Reynolds and coarse-graining hybrid decomposition or modified Lorenz-type spatiotemporal decomposition (Lorenz, 1967; Lu et al., 2016). Spatial scale separation uses a 2D boxcar sliding filter (Lu et al., 2016; Khani et al., 2019; Haigh et al., 2020) and can also be regarded as a coarse-graining method (Berloff, 2005; Aluie et al., 2018; Buzzicotti et al., 2021). The temporal scale separation is a Reynolds' average that was chosen to be the annual average in 2008. Hence, any field can be expressed as the sum of the instantaneous large-scale background field, SE field, and TE field as follows:

(9)

where [ ] represents the spatial filtered field, "-" represents the temporally averaged field, " " represents the eddy field that varies in space (the original field minus the spatially coarse-grained field), and " ' " represents the temporally varying eddy field (the original field minus the temporally averaged field). In this paper, the mesoscale eddy field is defined as a spatially varying small-scale field , which is assumed to be scale-separated from the large-scale background field and contains a stationary part and transient part . Accordingly, the mesoscale eddy flux can be decomposed into the SE flux and TE flux

(10)

This study focuses only on the influence of eddy flux that occurs completely inside the mesoscale or subgrid scale, namely, those in (10). When the coarse-graining method is used, the Leonard term (, describing the interaction within the resolved scale) and the Crank term (, describing the interaction between the resolved scale and the subgrid scale) appear because the scale separation conditions are not satisfied (Leonard, 1975; Clark et al., 1979; Bachman et al.,

2015). In this paper, we suppose spatial scale separation and do not consider these terms.

Then, we have the "flux-gradient" relationship of the total mesoscale eddy, SE, and TE as follows:

(11)

(12)

(13)

where

(14)

Namely, the transport tensor can also perform transient and stationary decomposition.

Thus far, we have formulated a diagnostic framework for the eddy transport process embracing transient/stationary (Reynolds and coarse-graining hybrid) decomposition and diffusion/advection (symmetric and antisymmetric) decomposition. All tensors and their elements will be discussed in this work.

2.3 Data and processing

In this paper, we show results only using Southern Ocean State Estimate (SOSE) eddy-permitting data from 2008 with a horizontal resolution of 1/6° for comparison with Lu et al. (2016). The research area is in the Southern Hemisphere south of 25°S. We also check the results of the eddy-resolving version of the LASG/IAP Climate System Ocean Model (LICOM; Liu et al., 2012 and Li et al., 2021) and obtain consistent diagnostic outcomes with SOSE. However, we do not show these results here.

For the hybrid framework, Reynolds' average is the annual average, and the coarse-graining method for spatial scale separation is a 3°×3° 2D boundary adaptive boxcar filter. When far from the boundary, the filter size is 3°×3°. When approaching the topographic boundary, the box's radius is automatically reduced to maintain the square shape (Lu et al., 2016; Haigh et al., 2020); its mathematical expression is

(15)

where and are the radii of the boxcar filter, and in this square case .

We choose to use the potential vorticity (PV,) to diagnose the eddy transport process. The diagnostic framework in this paper is carried out on isopycnal surfaces. The velocity field is interpolated to the density coordinate. The active tracer PV is calculated in the z-coordinate and then interpolated into the density coordinate. The filtering and gradient operations are entirely conducted along isopycnals. The advantage of this is that the problem can be simplified to a 2D problem, changing the transport tensor from rank 3 to rank 2. Then, we calculate all eddy fluxes and large-scale background PV gradients based

on (9)-(15) and estimate the transport coefficient and tensor. After acquiring the estimates of the transport tensors corresponding to the TE, SE, and total eddy PV fluxes based on the "flux-gradient" relationship, we further derive the following tensors through mathematical operations (3)-(7).

The specific step of the transport tensor estimation is as follows. First, the large-scale background gradient field and eddy flux fields are diagnosed directly from the data. Next, for a given point, the large-scale background field gradient and corresponding eddy flux are taken for all the valid points in a box (same as our boxcar filter) and a least-square regression is performed to obtain the slope as the estimation of each element of the transport tensor at a given point, i.e.,

(16)

are specific eddy PV fluxes in the x and y directions, respectively. Then, symmetric and antisymmetric decomposition is carried out. Furthermore, the symmetric part is diagonalized to obtain the eigenvalues and eigenvectors. The estimation of the transport coefficient under the isotropic assumption is similar.

We highlight that our sampling method in a box can be used to solve the underdetermined transport tensor estimation issue (Bachman & Fox-Kemper, 2013; Bachman et al., 2015; Bachman et al., 2020), avoiding the use of multiple tracers. However, it must be assumed that the large-scale background field is smooth and varies slowly.

3 Results

3.1 Meridional eddy PV transport

The zonal mean total meridional eddy PV transport (Figure 1a) is generally equatorward in areas above 400 m and north of 65°S. Poleward PV eddy flux exists in the shallow layers near the Antarctic continent and at a depth of 1000-2000 m south of 45°S (i.e., below the jet core). The magnitude of deep layer transport below 2000 m is relatively small.

The stationary (Figure 1d) and transient (Figure 1g) components of the zonal mean eddy PV transport are close in magnitude but have obviously different distributions. From an overall view, TEs account for most of the total PV transported to the equator, especially above the jet core. In shallow layers near the Antarctic continent, the distribution of SE flux is much more chaotic than that of TE flux. This difference is evidently related to the complicated topography. Both components have consistent equatorial transport in the upper layer far from the Antarctic continent, but the transient component is stronger, more coherent, and extends deeper downward. Both the TE and SE parts exhibit PV transport to the polar region at a deeper level, but their specific latitudes and depths are significantly different. The large value of the stationary component transported poleward is distributed at a depth of approximately 400 m to the south of the jet core near 60°S and may reach the bottom vertically. The transient component is strongly transported to the pole near 1000 m to

the north of the jet core, but with a smaller range. In deeper places, the PV transport is very weak.

As mentioned above, a prominent feature of the zonal mean stationary component is the strong poleward transport near the jet core (approximately 60°S and 400 m depth). We further select four potential density surfaces at $2 =$ 36.04, 36.38, 36.62, and 36.83 kg/m^3 to investigate the horizontal and vertical patterns of the stationary part (Figure 2). Noticeably, the large-value areas of meridional eddy PV transport on all isopycnals are closely related to the large-scale topography, such as the Kerguelen Plateau in the South Indian Ocean, the Mecquade Ridge extending from the Antarctic continent to the Pacific, and the complicated topographic distribution near the Antarctic Peninsula and the Drake Strait. Some studies have revealed several ways through which topography may affect the transport process. The topography can affect the jet structure and produce leaky jets in some places, destroying the blocking effect of the jets with cross-stream mixing, therefore enhancing the mixing process (Garabato et al., 2011; Thompson & Garabato, 2014). The topography may also stimulate stronger eddy activity and higher eddy kinetic energy (EKE) downstream, thus enhancing the eddy transport process (Thompson & Sallee, 2012). In addition, the topography forces the environmental PV contour to bend and modify the PV gradient to influence the performance of jet flow and eddy transport (Chen & Kamenkovich, 2013; Radko & Kamenkovich, 2017; Rhines, 2007; Thompson, 2010). The topographic effect also leads to a stronger local baroclinic instability by generating more extended meander contours and enhancing local buoyancy gradients, driving strong transient eddy activity to enhance transport (Abernathey & Cessi, 2014).

In addition, some large-value areas that are possibly related to large-scale topographies penetrate to a certain degree in the vertical direction, such as 80°E, 150°E and 50°W along the 60°S latitude circle; however, such areas may be affected by other nonconservative processes when close to the upper boundary (Treguier et al., 1997; Treguier, 1999).

3.2 The isotropic assumption

This section will investigate the transport coefficient based on the flux-gradient relationship under the isotropic assumption. Attention is given to the distribution and characteristics under stationary and transient decompositions.

3.2.1 The isotropic eddy transport coefficient

Under the isotropic assumption, most zonally averaged total eddy PV transport coefficients are positive and weakly negative only in a few regions (Figure 3). A negative transport coefficient actually corresponds to upgradient transport (Holland & Rhines, 1980; Lu et al., 2016; Rhines & Holland, 1979; Treguier et al., 1997; Wilson & Williams, 2006) but does not necessarily represent the existence of an anti-diffusion process. Nonlocal processes, such as the advection of tracer variance, destroy the locality hypothesis of the flux-gradient relationship, resulting in negative coefficients in diagnoses based on this assumption (Bach-

man & Fox-Kemper, 2013; Lu et al., 2016; Treguier et al., 1997). In addition, the SE flux can also contribute to the negative coefficient (Lu et al. 2016 and Figure 4 in this paper).

Under the jet core, i.e., at a depth of 1000-2000 m at approximately 50°S, there is significant mid-level lateral mixing enhancement. From the northern flank of the Antarctic Circumpolar Current (ACC) to the westward flow area, surface lateral mixing enhancement emerges. The TE mainly causes enhancement phenomena (see Figure 3c), consistent with previous studies (Abernathey et al., 2013; Garabato et al., 2011; Lu et al., 2016; Nikurashin & Ferrari, 2010; Treguier, 1999). Nikurashin and Ferrari (2010) and Garabato et al. (2011) explained the phenomena theoretically, showing that the local mixing length at the upper jet core can be reduced due to eddy propagation relative to the mean flow, resulting in a mixing suppression effect. Therefore, the lateral mixing is stronger in the westward flow area and to the northern side of the jet core.

From the zonal average, the transient part dominates the magnitude and structure of the isotropic transport coefficient, and the stationary transport coefficient is much smaller than the that of the transient part in most regions. This feature seems to contradict the importance of the meridional stationary eddy PV transport presented in the previous section. Because the zonal average loses much local information, the averaged transport coefficient is obviously underestimated. It can be seen from the horizontal map (Figure 4) that the local stationary transport coefficient can exceed 2000 m^2/s, which is similar to the horizontal order of the transient part, while both of these values rarely exceed 400 m^2/s after the zonal average. The substantial variation in the horizontal direction means that it is not proper to design the eddy transport parameterization scheme based only on the macrozonal mean structure.

In addition, concerning the SE transport coefficient (Figure 3b), we pay special attention to two places: the near-surface area to the north of 55°S and the area at approximately 1000 m in depth at 36°S. First, we believe that the stationary component represents near-surface nonconservative steady processes rather than topographic dominance. If this component is related to topography, it would be unlikely to span such an extensive range meridionally, and there is not a more coherent response at a deeper level. This means that the stationary part under the diagnostic framework of this paper is not entirely equivalent to the topographic effect, and the influence of near-surface nonconservative processes on mesoscale stationary eddy transport should not be ignored. Second, there is a dipole structure in the stationary transport coefficient. The horizontal distribution (Figure 4) is mainly due to the strong local transport coefficient enhancement by the large-scale topographies near South Africa, southwestern of Australia, and east of New Zealand. This topographic effect varies for different potential density layers. A similar structure is also found in the later anisotropy analysis.

Furthermore, taking a closer look at the horizontal distribution of the stationary transport coefficient (Figure 4), we find strong flaky large-value areas staggered

near the large-scale topographies. However, in other places, especially in the jet zone, the magnitude is not that strong. In the later anisotropic section, we will illustrate that the transport tensor diagnosed with a more complex anisotropic framework can be used to highlight the contribution of the stationary part in the topographic area and strong flow area, whether for the horizontal distribution or zonal average. Therefore, we assume the reason for the weak isotropic stationary transport coefficient is the inapplicability of the isotropic assumption; that is, it fails to effectively capture and fully express the mesoscale stationary eddy effect. In fact, the transport coefficient evaluated from the isotropic hypothesis represents the relationship between the length of the eddy flux vector and the length of the gradient vector, which naturally leads to the tangling of information in different directions, thus making the result less physically coherent. The negative transport coefficient actually represents the upgradient flux (from smaller to larger values). When the eddy tracer variance varies dramatically along the mean tracer contours, an upgradient flux or negative transport coefficient must appear in certain areas (Lu et al., 2016; Rhines & Holland, 1979; Treguier et al., 1997; Wilson & Williams, 2006).

3.2.2 The isotropic reconstruction

Figures 1b, 1e, and 1h show the zonally averaged meridional eddy PV transport reconstructed from the isotropic flux-gradient relationship, namely, . The reconstruction outcomes are not good compared to the diagnostic "true" field in Figures 1a, 1d, and 1g; these outcomes have an obvious distortion in the spatial distribution. Especially near the jet, there are large deviations in shape, extension depth, and north-south span, and at many places these values are even one order of magnitude smaller. The pattern correlation coefficient between the reconstructed zonal mean total meridional eddy transport and the diagnostic value is only 0.05. The error of the reconstruction results of the stationary part is slightly greater (the pattern correlation is -0.02), indicating that the isotropic hypothesis is not valid in the eddy transport process of the Southern Ocean considering stationary motion, resulting in the dramatic underestimation of the stationary part's contribution. The distribution of transient isotropic reconstruction is slightly more similar to the diagnostic field. The pattern correlation of the two zonal mean fields is 0.59, but the magnitude is still too small. For the horizontal distribution of isotropic reconstruction (Figure S1), although the reconstructed meridional transport is strong in the topographic and vigorous-flow areas, the distribution and intensity are in low agreement with the diagnostic distribution and intensity. The above results prove again that the isotropic hypothesis has a large deviation in its description of the mesoscale eddy process in the Southern Ocean, particularly for SEs.

3.3 The anisotropic assumption

This section will first examine all four elements of the transport tensor based on the flux-gradient relationship under the anisotropic assumption. We will investigate the characteristics of each tensor element obtained under the framework of "symmetric and antisymmetric" (or diffusion and advection) decomposition

and "stationary and transient" (or Reynolds and coarse-graining hybrid) decomposition. Then, the eigenvalues and eigenvectors of the symmetric part of the transport tensor will also be analyzed. We will investigate the eddy flux field reconstructed by the transport tensor through the flux-gradient relationship under the anisotropic framework.

3.3.1 The transport tensor

(1) Kxx

The zonal average of the first diagonal element Kxx of the total anisotropic transport tensor (Figure 5a) shows mid-layer mixing enhancement below the jet core near 50°S and surface layer enhancement to the north, consistent with the isotropic transport coefficient. The total Kxx is positive in most places, but strong negative values still exist in a few places, such as inside the jet core near 50°S. The transient part primarily contributes to the total Kxx distribution holistically (Figure 5c), while the stationary component (Figure 5b) exhibits a scattered pattern and remarkably modifies the total pattern only in limited areas where the intensity is relatively high. As we have pointed out above, the zonal mean underestimates the effects of the local pattern, so it should not be asserted that the stationary part of Kxx is less important than the transient part, particularly on the local scale. In fact, we can see from the horizontal distribution of the stationary Kxx (Figure 6) that its magnitude exceeds 2000 m^2/s in many places, similar to the horizontal distribution of the transient part. The zonal average undoubtedly weakens the result by one order of magnitude.

We next further investigate the Kxx stationary part. From its zonal average (Figure 5b), we first focus on the area near the surface and north of 55°S, where the stationary Kxx has a continuous large-value band consistent with the isotropic stationary coefficient. Here, we believe it represents the contribution of the near-surface nonconservative process to mesoscale SE transport. This indicates that the stationary part should not be completely equivalent to the topographic effect even in the anisotropic framework, especially in the near-surface region. We then take a closer look at the strong dipole of the stationary Kxx at 36°S and 1000 m depth; this dipole is also found in the stationary transport coefficient but is more intense here. From the horizontal distribution (Figure 6), we see that this strengthened dipole is related to the large-value area south of the African and Australian continents, showing that the stationary part can be related to the topography far away from the surface layer. For the patterns in different potential density layers, the large-scale topography exerts a vertically varying effect, as in the isotropic case.

In addition, from the horizontal distribution (Figure 6), there are flaky large-value areas near large-scale topographies and staggered positive and negative blocks on the ACC pathway. This demonstrates that the transport tensor diagnosed by the anisotropic framework has the ability to reasonably describe the contribution of the stationary part in the topography and energetic flow region, and this advantage will become more evident as we go through all elements of

the transport tensor later.

(2) Kxy

Under the assumption of anisotropy, the pattern of zonally averaged transport tensor elements Kxy (Figures 7a, 7b, and 7c) is completely distinguished from that of Kxx and the isotropic transport coefficients. The first distinction is that the large-value area's holistic distribution differs from both Kxx and . The total Kxy and its transient and stationary components have large values mainly concentrated within the upper 1000 m depth. These values are very small south of 60°S and in the deep ocean, unlike Kxx and , whose large values can extend to nearly 3000 m. The second distinction is that the specific distribution between Kxy and Kxx is entirely dissimilar. The total Kxy has a continuous positive area in the near-surface layer to the north of the jet core and a strong negative area between depths of 400 and 1000 m. This feature of the sharp contrast between the upper positive and lower negative is reflected in both the stationary part and the transient part. The third distinction is that the contributions of transient and stationary components are basically of equal importance (Figures 7b and 7c), and the stationary component is dominant in the upper ocean and in places intensely affected by large-scale topographies.

To further investigate the zonal average (Figure 7b) and horizontal distribution (Figure 8) of the stationary part, it is not difficult to reach the same conclusion as that from Kxx. The stationary part away from the surface is related to the topographic effect that exerts a changeable influence on the flow properties of different potential density layers. Looking more closely at the zonal mean Kxy stationary part, we perceive an asymmetric dipole composed of a larger and more intense positive area on the upper left and a smaller and weaker negative piece on the lower right. As mentioned before, the Kxx stationary part (Figure 5b) is an almost vertical positive and negative pair. The stationary part of another off-diagonal element, Kyx (Figure 7e), is also an asymmetric dipole but with smaller and weaker positive values in the upper left. The stationarity of the last element, Kyy (Figure 9e), has a nearly horizontal pair. These results reflect another advantage of the anisotropic framework: different elements of the stationary transport tensor might capture the topographic effect and the role of the stationary processes and decouple these effects from the different directions. In addition, from the horizontal distribution of stationary Kxy (Figure 8), the anisotropic transport tensor can reasonably describe and outstand the contribution of the stationary part in large-scale topographic areas and vigorous-flow areas.

(3) Kyx

Another off-diagonal element (Kyx) of the transport tensor (Figures 7d, 7e, and 7f) is generally weaker than Kxx and Kxy. The large-value areas of Kyx are distributed in the near-surface layer and upper-middle layer to the north of 60°S, and the stationary component is dominant. Comparing the zonally averaged total Kxy and Kyx (Figures 7a and 7d), both have intense positive values in the

surface layer north of 50°S, while decreasing positive values and large areas of strong negative values appear in Kxy. An approximate reverse pattern emerges in Kyx. The strong positive values of the surface are mainly supported by the stationary component, which is consistent with the previous consideration that the near-surface nonconservative processes rendering the stationary part should not be equivalent to the topographic effect. The overall distributions of Kxy and Kyx below the surface layer seem to have a certain degree of antisymmetry, which will become clearer when discussing symmetric and antisymmetric decomposition later.

The zonal mean stationary and transient Kyx and Kxy (Figure 7) have an upper-mid-layer strengthening phenomenon at the jet core below 400 m near 50°S. The isotropic transport coefficient and the middle layer enhancement in Kxx and Kyy are mainly manifested in the transient component, so the strengthening of Kyx and Kxyis unlikely to be the same. From the horizontal distribution of the stationary Kxy and Kyx (Figures 8 and S2), we find that the upper-mid-layer strengthening at 50°S is manifestly associated with the jet path, suggesting that large-scale flow structures such as the ACC can also contribute much to the stationary part. Therefore, the stationary tensor should not be assumed to be entirely equivalent to the topographic effect in the jet core region. Furthermore, the contribution of the ACC to the off-diagonal element of the stationary transport tensor also varies vertically. Although we leverage the Reynolds and coarse-graining hybrid diagnostic framework to perform the former analysis, at this point we cannot determine a concrete physical mechanism to comprehend this phenomenon.

(4) Kyy

The zonal average of another diagonal element of the total transport tensor Kyy is consistent with Kxx and the isotropic transport coefficient (Figures 5a, 5d, and 3a). They all have mid-level enhancement below the jet core and surface enhancement to the north. The transient component can be used to roughly outline the total Kyy and is positive in most places (Figure 5f). The stationary part (Figure 5e) modifies the distribution of the total Kyy, especially in the near-surface layer north of 60°S and between 30°S and 40°S.

Similarly, a large-value region of stationary Kyy also appears near 36°S, and it is a dipole structure tending to the horizontal direction with negative values in the north and positive values in the south. As discussed above, these results may indicate that different elements of the stationary transport tensor can capture the influence of the topography on the flow field in different directions, reflecting the advantages of the anisotropic framework. Regarding the large-scale topography effects on the transport tensor, we consider it one of the directions for applying our diagnostic framework in the near future.

To sum up, the anisotropic assumption is consistent with the actual physical process and necessary in mesoscale eddy parameterization; primarily, it captures the importance of SEs to the transport tensor. Large-scale topographies,

nonconservative processes, and large-scale vigorous flow structures may all affect the stationary transport tensor, and the impact is anisotropic horizontally and varies vertically. In addition, the nonconservative processes have a notable influence on the near-surface stationary tensor, and it seems difficult to disentangle the effect of a large-scale flow structure on the stationary tensor from the topographic effect.

3.3.2 The symmetric and antisymmetric decomposition

We will decompose the transport tensors into their symmetric and antisymmetric components and examine the features of the off-diagonal elements.

1. **The antisymmetric component**

The antisymmetric part of the anisotropic transport tensor is determined by its off-diagonal element Axy (because Ayx = -Axy). Its zonal mean (Figures 9d, 9e, and 9f) is holistically similar to that of Kxy, such as positive bands at a depth above 400 m and negative bands at a depth of 400-1000 m. However, the corresponding magnitude is smaller than Kxy, which is consistent with the fact that the absolute value of Kxy is generally larger than that of Kyx.

Transient and stationary Axy are of similar order and, after synthesizing the information of Kyx and Kxy, show a clearer upper-mid enhancement of approximately 1000 m at 50°S below the jet core. In the horizontal pattern of stationary Axy in Figure S4, we see that the upper-mid enhancement of 50°S is related to the jet path, indicating that a large-scale flow field structure such as the ACC may have a vertically varying contribution to the stationary part of the advection process (or skew flux) along the tracer contours represented by Axy.

There is only one strong positive region in the zonally averaged stationary Axy at a depth of approximately 1000 m at approximately 36°S; this is quite different from the asymmetric dipole of the transport tensor's four elements and the symmetric dipole of the symmetric tensor found in the next section. This difference shows that large-scale topography can affect the anisotropy of the transport tensor by affecting the stationary part of the antisymmetric tensor or the stationary advective process accordingly.

In addition, from the horizontal distribution of Axy (Figure S4), we find that the topographies near Africa, Australia, New Zealand, and South America produce strong Axy-positive areas. Compared with bathymetry, these positive Axy areas tend to occur in shallow and adjacent downstream regions. However, the relationship between specific topographic quantities (such as topography variance or slope) and Axy is unclear (not shown). The synergistic effect of multiple topography-related quantities likely determines the impact of topography on the antisymmetric tensor. The path of the direct topography effect on the transport tensor needs to be investigated in future research.

(2) The symmetric component

The zonal mean (Figures 9a, 9b, and 9c) of the off-diagonal symmetric tensor element Sxy is smaller than those of Kxy and Kyx. The stationary part of Sxy makes a decisive contribution to the total Sxy. So far, a common feature of the transport tensors and the corresponding symmetric and antisymmetric components obtained in this paper is that their off-diagonal contributions to the stationary process are relatively large. The magnitude of Sxy is holistically much less than those of Kxx and Kyy (i.e., Sxx and Syy). This difference might indicate that the latitudinal and meridional directions are generally the two characteristic directions of ocean mesoscale motion. Nevertheless, the statement is not robust based on the eigenanalysis of symmetric tensors in section 3.3.3, which will investigate the horizontal patterns of eigenvalues and eigenvectors.

For computational convenience, one may take Sxy = Axy (Smith & Gent, 2004), but this assumption is unreasonable. Although the zonal means Axy and Sxy (Figure 9) are of almost the same order, their distributions are quite inconsistent, whether in the jet region, near-surface area, or topographic area. In particular, we note that there is only one positive-value area of stationary Axy at a depth of about 1000 m near 36°S, while the stationary part of Sxy at the corresponding position is an upper and lower dipole slightly inclined in the vertical direction. Thus, we consider that the symmetric and antisymmetric components describe independent processes. In other words, we may regard Axy and Sxy as capturing different sides of stationary eddy behavior, especially considering the topographic effect.

1. The eigenanalysis of the symmetric tensor

In this section, we diagonalize the symmetric tensor to obtain eigenvalues and eigenvectors and to analyze their spatial distribution and the configuration relationship between eigenvalues.

The major eigenvalue and eigenvector

The zonal mean total, transient, and stationary major eigenvalues (Figures 10a, 10b, and 10c) are positive in the domain, indicating "positive diffusion" that weakens the eddy PV variance along the major axis. The total eigenvalue decreases monotonically from top to bottom and from north to south. There is no mid-level enhancement phenomenon in the jet zone but only a surface enhancement phenomenon on the northern flank of the ACC and near the surface of the westward flow. We maintain that the mid-layer enhancement is the enhancement of lateral mixing perpendicular to the jet flow direction. Because the eigenvalue represents the mixing intensity in the eigendirection and the base vectors of the tensor after diagonalization become eigenvectors that no longer coincide with the longitude or latitude, the zonal mean eigenvalue inherently lacks rationality and physical explanation. Therefore, the investigation of eigenvalues and eigenvectors needs to be done horizontally.

Figures 11a, 11b, and 11c show the major eigenvalue distributions and their characteristic directions on selected potential density layers of $2 = 36.83$ kg/m3. The major eigenvalues in most areas are positive. However, there are still a few

negative values, and the strong negative values are related to the ACC pathway and large-scale topography. Both stationary and transient components may have negative-value areas, and their positions do not seem to be linked in any way. The stationary part is weaker than the transient part as a whole, but its contribution is still remarkable. Both components tend to increase in energetic flow areas and near large-scale topographies.

(2) The minor eigenvalue

Most zonal mean minor eigenvalues (Figures 10d, 10e, and 10f) are negative. The stationary parts are all negative, while the transient and total parts are positive only in limited places, such as below 2000 m. Further investigating the horizontal distribution of the minor eigenvalues (Figures 11d, 11e and, 11f, the $2 = 36.83$ kg/m^3 layer is selected, and the results in other layers are similar), we find that the minor eigenvalues are negative in a large proportion of the domain. However, there are still some places with strong positive minor eigenvalues. The positive area is mainly supported by the transient component. We also discover great uncertainty in the relationship between the positive-area distribution and the large-scale topography and jet path for the transient and stationary parts. We feel it is likely that there are strong positive minor eigenvalues inside strong current areas and the downstream sides of large-scale topographies. We also point out that the absolute values of the zonal mean transient, stationary, and total minor eigenvalues (Figures 10d, 10e, and 10f) reach their maxima in the northern flank of the jet core at a depth of approximately 400 m. Positive eigenvalues represent a weakened tracer variance along the corresponding characteristic direction, while negative eigenvalues indicate the opposite trend. Combined with the positive major eigenvalue results, we believe that the strong polarization feature of eigenvalues in the places mentioned above represents a strong filamentation process (Ledwell et al., 1998; Haigh et al., 2020; Haigh et al., 2021a; see also part (3) in this section). In addition, in the westerly flow area on the northern side of the ACC, the eddy mixing of the transient part is strengthened at the surface; this is consistent with Tulloch et al. (2011) and Khani et al. (2019), who demonstrated that the eastward trade wind supports shallow baroclinic modes at that location.

(3) Configuration of eigenvalues

Based on Wilson and Williams (2006), the eigenvalue contributions to the perturbation tracer variance can be obtained, i.e.,

(17)

where and are the gradients of the large-scale PV field in the major and minor characteristic directions, respectively. Here, the prime symbol represents the perturbation quantity, which can be regarded as the mesoscale eddy field in this paper.

Since the major eigenvalue must be larger than the minor eigenvalue, there are three scenarios:

1) The major eigenvalue is positive, and the minor eigenvalue is negative (major+&minor-), indicating that either the tracer variance or PV enstrophy is reduced by "positive diffusion" in the major characteristic direction and increased by "negative diffusion", or anti-diffusion, in the minor one. In other words, the process of filamentation has taken place (Ledwell et al., 1998; Haigh et al., 2020; Haigh et al., 2021a). This is the most common case, whether stationary, transient, or at different layers (Figure 12) and is dominant in the jet area and at the west boundary (Figure 11). Recent research, including Stanley et al. (2020), Haigh et al. (2020), and Haigh et al. (2021a), has made a similar discovery.

2) Both the major and minor eigenvalues are positive (major+&minor+), indicating that the tracer variance increases on the plane supported by the two eigenvectors. This also means that these geographical places are complete sources of PV enstrophy and tend to constantly stimulate eddy activity. This situation occurs mostly on the north flank of the jet stream and to the west of the large-scale topography, with a few occasional spots inside the ACC. The transient component is slightly more prone to this situation than the stationary component (Figures 12b and 12c). The positive minor eigenvalue can be very strong, which implies that transient eddies are the dominant process for starting or strengthening the activities of the ocean mesoscale system.

3) Both eigenvalues are negative (major-&minor-), indicating that the tracer variance decreases in both characteristic directions; this creates either sinks of eddy PV enstrophy or a tendency to kill eddy activity. This scenario occurs very rarely and is prone to being embedded in the strong flow region (Figure 12).

In summary, three configurations of the symmetrical part eigenvalues of the transport tensor all appear in the Southern Ocean. We highlight that the major+&minor- configuration is the most frequent and represents the dominance of the filamentation process, which can be reflected by the stationary and transient parts and different vertical layers.

(4) The absolute angle analysis for eigenvectors

Here, we will calculate the absolute angle between the major eigenvector (to which the minor eigenvector is perpendicular) and a selected physical quantity (such as the PV gradient, velocity vector, and topographic slope vector), rather than the angle's cosine value calculated Bachman et al. (2020).

Figure 13 shows the horizontal distribution of the absolute angle between the total major eigenvector and either the large-scale PV gradient, large-scale velocity vector, or topographic slope vector on a selected potential density layer ($2 = 36.38$ kg/m^3). In the whole domain, the absolute angle may change from 0° to 90°; the corresponding vectors may be almost parallel or completely orthogonal. We find it difficult to summarize an applicable empirical rule regarding when or where these vectors tend to be parallel or orthogonal. This result seems to contradict Bachman et al. (2020) in that the major eigenvector is parallel to

the velocity vector or perpendicular to the PV gradient. We re-examine the results in Bachman et al. (2020) and find that they compute the cosine value, which is not linear with the absolute angle. For example, when the cosine value is 0.85, the included angle is already 30°, which obviously cannot be considered parallel. In the results of Bachman et al. (2020), there are large areas where the cosine value of the angle between the major eigenvector and the velocity vector is lower than 0.85, indicating that most places do not fit their conclusion that the major eigenvector is parallel to the velocity vector. Therefore, this paper and Bachman et al. (2020) demonstrate that the angle between the eigenvector and either the PV gradient, the velocity vector field, or the topographic slope (all on a large scale) has no global unified feature but has a certain degree of randomness.

Further comparing the absolute included angle between the major eigenvector and the PV gradient on two density layers (2 = 36.38 and 36.62 kg/m3 in Figures 13a and 13f, respectively), we observe not only that the horizontal pattern in each layer looks quite random but also that there is no global consistency between these two layers. In addition, from Figures 13a, 13d, and 13e, the absolute angle analysis under stationary and transient decomposition fails to produce a more orderly structure but proves the randomness.

Figure 14 shows the vertical profile of the probability density function (PDF) of the absolute angle between the major eigenvector (including the total, stationary and transient components) and either the large-scale PV gradient, velocity vector, or topographic slope. Although we can see that the PDF of some quantities seems to prefer a skewed distribution, caveats should be considered because the value difference between the blackest and whitest color is insufficiently large (the difference is approximately only a quarter of the PDF represented by the whitest color). Thus, this nonuniformity does exist but is fairly weak. In addition, the intermediate angle (20°-70°) accounts for a large proportion, implying that the PDFs might be considered to add weak nonuniformity to a uniform distribution. A uniform distribution here means a high randomness of the absolute angle, where the nonuniformity perhaps represents the corresponding physical relations. That is, the PV gradient, velocity field, and topography should affect the direction of the major eigenvector. We speculate that the determination of the eigenvector might involve an intricate and highly sensitive process; namely, multiple physical quantities can affect the eigenvector, and the final orientation depends on the residual of all effects. Therefore, in terms of spatial distribution and even time evolution, the drastic change in the dominance of each physical quantity and its underlying physical mechanism would produce the high randomness of the eigenvector. These results further suggest a possible parameterization scheme of eddy diffusion, based on the eigenmatrix and eigenvectors, in which some stochastic factors are introduced. These factors include taking random numbers from a predefined or diagnostic PDF to specify the angle between the major eigenvector and a certain quantity, such as a large-scale velocity vector, so that the characteristic direction can be flow-dependent.

3.3.4 The anisotropic reconstruction

This section will investigate the reconstruction of meridional eddy PV transport using tensor elements Kyx, Kyy, Ayx, and Syx and their combination under the anisotropic framework; this will then be compared with the isotropic reconstruction results.

The reconstruction result for the anisotropic transport tensor (i.e.,) is the best (Figures 1c, 1f, and 1i); it is much better than any single tensor element and the isotropic coefficient (Figures 1b, 1e, and 1h). This once again proves that the anisotropic hypothesis is more reasonable than the isotropic hypothesis at the mesoscale.

The reconstruction by only the off-diagonal element Kyx of the transport tensor (i.e.,) is shown in Figures S6a, S6b, and S6c. The pattern correlation of the total transport is 0.416. The reconstructed field bears similarity only with the diagnostic area in the upper ocean and deviates greatly in the jet region. The results reconstructed by only the diagonal element of the transport tensor Kyy (i.e.,) are shown in Figures S6d, S6e, and S6f. The pattern correlation of the total transport is 0.526. The similarity between the reconstructed field and the diagnostic field is visually higher than that of Kyx.

The transport reconstructed by the antisymmetric tensor's off-diagonal element Ayx (i.e.,) is shown in Figures S7a, S7b, and S7c. We find trivial patterns, and the magnitude is one order smaller. The reconstructed transport under the zonal average is very weak, so it is doubtful that the zonal average would significantly underestimate the contribution of the skew flux. After all, the magnitude of Axy is comparable to that of any element in the transport tensor K. However, from the horizontal distribution of the Ayx reconstruction (not given), the meridional advective flux is indeed weak, and there are a handful of positive-negative large-value pairs that may offset each other in a zonal circle.

The contribution of the symmetric part off-diagonal elements to the meridional eddy transport (i.e., , Figures S7d, S7e, and S7f) is weak and modifies only the pattern. Comparing the reconstructions by symmetric and antisymmetric tensors, the transient parts are similar, while the stationary parts are quite different. This result implies that the effects of the transient part of the symmetric tensor (eddy diffusion) and the antisymmetric tensor (eddy advection) on meridional eddy transport may compound, while the stationary parts tend to be independent of each other, and the stationary and transient parts are of no association.

is the reconstruction of the diffusive part of the eddy flux with the complete symmetric tensor (Figures S8a, S8b, and S8c). The zonal average generates decent qualitative and quantitative outcomes, with a pattern correlation of 0.642 between the total reconstruction field and the diagnostic field. Although this construction represents most features, there is a deviation near the jet core, and the stationary result is slightly worse than the transient result. However, after adding the contribution of the antisymmetric tensor that makes a systematic

correction, namely, (Figures S8d, S8e, and S8f), we unsurprisingly obtain the best reconstruction result; the pattern correlation of the total scenario reaches 0.873.

Rotation, stratification, and topographic effects make mesoscale oceanic flow anisotropic. Thus, the anisotropic hypothesis is more physically aligned with the real world than the isotropic hypothesis. In addition, we find that the meridional eddy PV transport reconstructed anisotropically is closer to the diagnostic value than that reconstructed isotropically. The anisotropic framework can capture the effects of the stationary eddy, especially the topographic effect. Therefore, it is more suitable to make the anisotropic assumption for the parameterization of mesoscale eddy transport.

4 Summary

In this paper, we have proposed a Reynolds and coarse-graining hybrid eddy transport diagnostic framework, in which a coarse-graining method for spatial scale separation and a Reynolds' time average for temporal separation are applied in the Southern Ocean. The mesoscale variability is defined as the relatively small-scale deviation from the large spatial scale background field and can be further decomposed into stationary and transient eddies in our framework. We then diagnose the isotropic transport coefficient and anisotropic transport tensor using the "flux-gradient" relationship, split the tensor into its symmetric and antisymmetric parts, and analyze the eigenvalues and eigenvectors of the symmetric tensor.

We verify that the anisotropic assumption is more reasonable than the isotropic assumption for the ocean mesoscale eddy transport process. In addition to higher alignment with the physical features of real-world ocean mesoscale flow, the anisotropic assumption leads to the reconstruction of meridional PV transport that is much closer to that of the diagnostic field. The anisotropic framework can capture the effect of stationary eddies and shed some light on the potential topography influences on the transport tensor and coefficient.

Because the effect of the stationary eddy is currently under insufficient discussion, we pay particular attention to its contribution to the transport tensor under our hybrid framework. Large-scale topographies, nonconservative processes, and large-scale flow structures can affect the stationary transport tensor, where this influence is highly horizontally anisotropic and has a vertical structure. The nonconservative process has a great impact on the stationary tensor in near-surface areas. Although it seems difficult to decouple the large-scale structure (e.g., the ACC jet core) effect on the stationary component from the purely topographic structure, the stationary and symmetrical part of the transport tensor is substantially modulated by topography. In addition, a common feature of the transport tensor and its symmetric and antisymmetric components is that the contribution of the stationary part to their off-diagonal elements is dominant.

Compared with Lu et al. (2016), the work in this paper further decomposes the

transport tensor symmetrically and anti-symmetrically and probes all tensor-related elements, especially the eigenvalues and eigenvectors of the symmetric part of the transport tensor. We find that three configurations of the major and minor eigenvalues of the symmetric tensor appear in the Southern Ocean, including major+&minor-, major+&minor+, and major-&minor-. These configurations represent vortex filamentation movement, the source of PV enstrophy, and the sink of PV enstrophy, respectively. Among them, major+&minor- is the most common case in the Southern Ocean. Although there are three eigenvalue polarity cases, the magnitude of the eigenvalues can still be determined in a sense. In addition, we find high randomness of the eigenvector by calculating the absolute angle between the eigenvector direction and either the PV gradient, velocity vector or topographic slope vector. This finding implies that the eigenvector may depend on a residual of various physical processes, so it is susceptible to the environment and shows randomness. These results may introduce random factors into the eddy diffusion parameterization scheme based on the eigenvalues and eigenvector. For example, one may set the approximate magnitude of the eigenvalue from the diagnosis results or a pre-existing scheme and take a random number from a well-defined probability density distribution to determine the angle between the eigenvector and some quantities, such as the velocity direction, to make the eigenvector flow-dependent.

This study also has some limitations. The first is the problem of data. To facilitate the comparison with Lu et al. (2016), we show the 1/6° eddy-permitting data results. However, we also use the eddy-resolving global ocean model with 0.1° horizontal resolution and obtain consistent conclusions. Although the data resolution does not cause great problems, both SOSE and the global eddy-resolving model contain too many physical processes, making it difficult to distinguish the impacts of specific mechanisms on the transport tensors (especially on eigenvectors). When studying the potential influence of the topography, we fail to give a specific dynamic mechanism of how the topography influences the transport tensor and decouples its effect from other processes. Therefore, our conclusions are only of enlightenment on a potentially new perspective about topography influence and parameterization. In the future, diagnosing and constructing parameterization schemes (deterministic or random parameterization) using a Reynolds and coarse-graining hybrid framework in this paper should be based on ideal numerical simulation to better control the variables. In addition, this paper assumes that the mesoscale and large-scale background fields meet the scale separation conditions, so the Leonard term describing the interaction within the resolved scale and the crank term describing the interaction between the resolved scale and the subgrid scale are not investigated. Both of these terms might be important, especially when increasing the horizontal resolution. Therefore, the future application of this diagnosis should consider the complete eddy flux, as in Haigh et al. (2021a).

Acknowledgments

The study was funded by the National Key Research and Development Pro-

gram (2018YFA0605703 and 2020YFA0608902), the National Natural Sciences Foundation (41931183 and 41976026), and the Strategic Priority Research Program of the Chinese Academy of Sciences (Grant No. XDB42010404). HLL and PFL were also supported by the "Earth System Science Numerical Simulator Facility" (EarthLab). Southern Ocean State Estimate (SOSE) eddy-permitting data can be found in https://climatedataguide.ucar.edu/climate-data/southern-ocean-state-estimate-sose. The data used in the figures can be obtained online (http://data.lasg.ac.cn/lhl/data-hybrid-framework/). We thank Jianhua Lu and Yihua Lin for their helpful discussion on the scheme.

References

https://doi.org/10.1016/j.ocemod.2021.101845

https://doi.org/10.1029/98JC01738

https://doi.org/10.1016/0377-0265(79)90015-0

Abernathey, R., & Cessi, P. (2014). Topographic Enhancement of Eddy Efficiency in Baroclinic Equilibration. *Journal of Physical Oceanography, 44*(8), 2107-2126. doi:10.1175/jpo-d-14-0014.1Abernathey, R., Ferreira, D., & Klocker, A. (2013). Diagnostics of isopycnal mixing in a circumpolar channel. *Ocean Modelling, 72*, 1-16. doi:10.1016/j.ocemod.2013.07.004Aluie, H., Hecht, M., & Vallis, G. K. (2018). Mapping the Energy Cascade in the North Atlantic Ocean: The Coarse-graining Approach. *Journal of Physical Oceanography, 48*(2), 225-244. doi:10.1175/jpo-d-17-0100.1Bachman, S., & Fox-Kemper, B. (2013). Eddy parameterization challenge suite I: Eady spin-down. *Ocean Modelling, 64*, 12-28. doi:10.1016/j.ocemod.2012.12.003Bachman, S. D. (2019). The GM E closure: A framework for coupling backscatter with the Gent and McWilliams parameterization. *Ocean Modelling, 136*, 85-106. doi:10.1016/j.ocemod.2019.02.006Bachman, S. D., Fox-Kemper, B., & Bryan, F. O. (2015). A tracer-based inversion method for diagnosing eddy-induced diffusivity and advection. *Ocean Modelling, 86*, 1-14. doi:10.1016/j.ocemod.2014.11.006Bachman, S. D., Fox-Kemper, B., & Bryan, F. O. (2020). A Diagnosis of Anisotropic Eddy Diffusion From a High-Resolution Global Ocean Model. *Journal of Advances in Modeling Earth Systems, 12*(2). doi:10.1029/2019ms001904Berloff, P. S. (2005). On dynamically consistent eddy fluxes. *Dynamics of Atmospheres and Oceans, 38*(3-4), 123-146. doi:10.1016/j.dynatmoce.2004.11.003Bischoff, T., & Thompson, A. F. (2014). Configuration of a Southern Ocean Storm Track. *Journal of Physical Oceanography, 44*(12), 3072-3078. doi:10.1175/jpo-d-14-0062.1Buzzicotti, M., Storer, B., Griffies, S., & Aluie, H. (2021). *A coarse graining decomposition of surface geostrophic kinetic energy in the global ocean.*Chen, C., & Kamenkovich, I. (2013). Effects of Topography on Baroclinic Instability. Journal of Physical Oceanography. *43*(4), 790-804. doi:10.1175/jpo-d-12-0145.1Clark, R. A., Ferziger, J. H., & Reynolds, W. C. (1979). Evaluation of subgrid-scale models using an accurately simulated turbulent flow. *Journal of Fluid Mechanics,*

91(1), 1-16. doi:10.1017/S002211207900001XDukowicz, J. K., & Smith, R. D. (1997). Stochastic theory of compressible turbulent fluid transport. *Physics of Fluids, 9*(11), 3523-3529. doi:10.1063/1.869460Fox-Kemper, B., Lumpkin, R., & Bryan, F. O. (2013). Chapter 8 - Lateral Transport in the Ocean Interior. In G. Siedler, S. M. Griffies, J. Gould, & J. A. Church (Eds.), *International Geophysics* (Vol. 103, pp. 185-209): Academic Press.Garabato, A. C. N., Ferrari, R., & Polzin, K. L. (2011). Eddy stirring in the Southern Ocean. *Journal of Geophysical Research-Oceans, 116*. doi:10.1029/2010jc006818Gent, P. R., & McWilliams, J. C. (1990). Isopycnal Mixing In Ocean Circulation Models. *Journal of Physical Oceanography, 20*(1), 150-155. doi:10.1175/1520-0485(1990)020<0150:Imiocm>2.0.Co;2Gent, P. R., Willebrand, J., McDougall, T. J., & McWilliams, J. C. (1995). Parameterizing Eddy-Induced Tracer Transports in Ocean Circulation Models. *Journal of Physical Oceanography, 25*(4), 463-474. doi:10.1175/1520-0485(1995)025<0463:Peitti>2.0.Co;2Griffies, S. M. (1998). The Gent-McWilliams skew flux. *Journal of Physical Oceanography, 28*(5), 831-841. doi:10.1175/1520-0485(1998)028<0831:Tgmsf>2.0.Co;2Griffies, S. M., Gnanadesikan, A., Pacanowski, R. C., Larichev, V. D., Dukowicz, J. K., & Smith, R. D. (1998). Isoneutral diffusion in a z-coordinate ocean model. *Journal of Physical Oceanography, 28*(5), 805-830. doi:10.1175/1520-0485(1998)028<0805:Idiazc>2.0.Co;2Haigh, M., Sun, L., McWilliams, J. C., & Berloff, P. (2021a). On eddy transport in the ocean. Part I: The diffusion tensor. *Ocean Modelling, 164*. doi:10.1016/j.ocemod.2021.101831Haigh, M., Sun, L., McWilliams, J. C., & Berloff, P. (2021b). On eddy transport in the ocean. Part II: The advection tensor. *Ocean Modelling, 165*, 101845. doi:Haigh, M., Sun, L., Shevchenko, I., & Berloff, P. (2020). Tracer-based estimates of eddy-induced diffusivities. *Deep-Sea Research Part I-Oceanographic Research Papers, 160*. doi:10.1016/j.dsr.2020.103264Holland, W. R., & Rhines, P. B. (1980). An Example of Eddy-Induced Ocean Circulation %J Journal of Physical Oceanography. *10*(7), 1010-1031. doi:10.1175/1520-0485(1980)010<1010:Aeoeio>2.0.Co;2Khani, S., Jansen, M. F., & Adcroft, A. (2019). Diagnosing Subgrid Mesoscale Eddy Fluxes With and Without Topography. *Journal of Advances in Modeling Earth Systems, 11*(12), 3995-4015. doi:10.1029/2019ms001721Ledwell, J. R., Watson, A. J., & Law, C. S. (1998). Mixing of a tracer in the pycnocline. *103*(C10), 21499-21529. doi:Lee, M. M., Marshall, D. P., & Williams, R. G. (1997). On the eddy transfer of tracers: Advective or diffusive? *Journal of Marine Research, 55*(3), 483-505. doi:10.1357/0022240973224346Leonard, A. (1975). Energy Cascade in Large-Eddy Simulations of Turbulent Fluid Flows. In F. N. Frenkiel & R. E. Munn (Eds.), *Advances in Geophysics* (Vol. 18, pp. 237-248): Elsevier.Li, Y. W., H. L. Liu, M. R. Ding P. F. Lin, Z. P. Yu, Y. Q. Yu, Y. Meng, Y. L. Li, X. D. Jian, J. R. Jiang, K. J. Chen, Q. Yang, Y. Q. Wang, B. W. Zhao, J. L. Wei, J. F. Ma, W. P. Zheng, and P. F. Wang, 2020: Eddy-resolving Simulation of CAS-LICOM3 for Phase 2 of the Ocean Model Intercomparison Project. Adv. Atmos. Sci., 37(10), 1067–1080. https://doi.org/10.1007/s00376-020-0057-z.Liu, H. L., P. F. Lin, Y. Q. Yu, and X. H. Zhang, 2012: The baseline evaluation of LASG/IAP Climate system Ocean Model (LICOM)

version 2. Acta Meteor. Sinica, 26(3), 318–329, doi: 10.1007/s13351-012-0305-y.Lu, J., Wang, F., Liu, H., & Lin, P. (2016). Stationary mesoscale eddies, upgradient eddy fluxes, and the anisotropy of eddy diffusivity. *Geophysical Research Letters, 43*(2), 743-751. doi:10.1002/2015gl067384MacCready, P., & Rhines, P. B. (2001). Meridional transport across a zonal channel: Topographic localization. *Journal of Physical Oceanography, 31*(6), 1427-1439. doi:10.1175/1520-0485(2001)031<1427:Mtaazc>2.0.Co;2Mak, J., Marshall, D. P., Maddison, J. R., & Bachman, S. D. (2017). Emergent eddy saturation from an energy constrained eddy parameterisation. *Ocean Modelling, 112*, 125-138. doi:10.1016/j.ocemod.2017.02.007Marshall, D. P., Maddison, J. R., & Berloff, P. S. (2012). A Framework for Parameterizing Eddy Potential Vorticity Fluxes. *Journal of Physical Oceanography, 42*(4), 539-557. doi:10.1175/jpo-d-11-048.1Marshall, D. P., Williams, R. G., & Lee, M. M. (1999). The relation between Eddy-induced transport and isopycnic gradients of potential vorticity. *Journal of Physical Oceanography, 29*(7), 1571-1578. doi:10.1175/1520-0485(1999)029<1571:Trbeit>2.0.Co;2McDougall, T. J. (1987). Neutral Surfaces In The Ocean: Implications For Modeling. *Geophysical Research Letters, 14*(8), 797-800. doi:10.1029/GL014i008p00797Nikurashin, M., & Ferrari, R. (2010). Suppression of Eddy Diffusivity across Jets in the Southern Ocean. *Journal of Physical Oceanography, 40*(7), 1501-1519. doi:10.1175/2010jpo4278.1Radko, T., & Kamenkovich, I. (2017). On the Topographic Modulation of Large-Scale Eddying Flows. *Journal of Physical Oceanography, 47*(9), 2157-2172. doi:10.1175/jpo-d-17-0024.1Redi, M. H. (1982). Oceanic Isopycnal Mixing By Coordinate Rotation. *Journal of Physical Oceanography, 12*(10), 1154-1158. doi:10.1175/1520-0485(1982)012<1154:Oimbcr>2.0.Co;2Rhines, P. B. (2007). Jets and Orography: Idealized Experiments with Tip Jets and Lighthill Blocking %J Journal of the Atmospheric Sciences. *64*(10), 3627-3639. doi:10.1175/jas4008.1Rhines, P. B., & Holland, W. R. (1979). A theoretical discussion of eddy-driven mean flows. *Dynamics of Atmospheres and Oceans, 3*(2), 289-325. doi:Smith, R. D., & Gent, P. R. (2004). Anisotropic Gent-McWilliams parameterization for ocean models. *Journal of Physical Oceanography, 34*(11), 2541-2564. doi:10.1175/jpo2613.1Stanley, Z., Bachman, S. D., & Grooms, I. (2020). Vertical Structure of Ocean Mesoscale Eddies with Implications for Parameterizations of Tracer Transport. *Journal of Advances in Modeling Earth Systems, 12*(10). doi:10.1029/2020ms002151Taylor, G. I. (1922). Diffusion by continuous movements. *Proceedings of the London Mathematical Society, 20*, 196-212. Thompson, A. F. (2010). Jet Formation and Evolution in Baroclinic Turbulence with Simple Topography. *Journal of Physical Oceanography, 40*(2), 257-278. doi:10.1175/2009jpo4218.1Thompson, A. F., & Garabato, A. C. N. (2014). Equilibration of the Antarctic Circumpolar Current by Standing Meanders. *Journal of Physical Oceanography, 44*(7), 1811-1828. doi:10.1175/jpo-d-13-0163.1Thompson, A. F., & Sallee, J.-B. (2012). Jets and Topography: Jet Transitions and the Impact on Transport in the Antarctic Circumpolar Current. *Journal of Physical Oceanography, 42*(6), 956-972. doi:10.1175/jpo-d-11-0135.1Treguier, A. M. (1999). Evaluating eddy mixing coefficients from eddy-resolving ocean models: A case study. *Journal of Marine*

Research, 57(1), 89-108. doi:10.1357/002224099765038571Treguier, A. M., Held, I. M., & Larichev, V. D. (1997). Parameterization of quasigeostrophic eddies in primitive equation ocean models. *Journal of Physical Oceanography, 27*(4), 567-580. doi:10.1175/1520-0485(1997)027<0567:Poqeip>2.0.Co;2Treguier, A. M., & McWilliams, J. C. (1990). TOPOGRAPHIC INFLUENCES ON WIND-DRIVEN, STRATIFIED FLOW IN A BETA-PLANE CHANNEL - AN IDEALIZED MODEL FOR THE ANTARCTIC CIRCUMPOLAR CURRENT. *Journal of Physical Oceanography, 20*(3), 321-343. doi:10.1175/1520-0485(1990)020<0321:Tiowds>2.0.Co;2Tulloch, R., Marshall, J., Hill, C., & Smith, K. S. (2011). Scales, Growth Rates, and Spectral Fluxes of Baroclinic Instability in the Ocean %J Journal of Physical Oceanography. *41*(6), 1057-1076. doi:10.1175/2011jpo4404.1Vallis, G. K. (2017). *Atmospheric and Oceanic Fluid Dynamics: Fundamentals and Large-Scale Circulation* (2 ed.). Cambridge: Cambridge University Press.Visbeck, M., Marshall, J., Haine, T., & Spall, M. (1997). Specification of eddy transfer coefficients in coarse-resolution ocean circulation models. *Journal of Physical Oceanography, 27*(3), 381-402. doi:10.1175/1520-0485(1997)027<0381:Soetci>2.0.Co;2Wilson, C., & Williams, R. G. (2004). Why are eddy fluxes of potential vorticity difficult to parameterize? *Journal of Physical Oceanography, 34*(1), 142-155. doi:10.1175/1520-0485(2004)034<0142:Waefop>2.0.Co;2Wilson, C., & Williams, R. G. (2006). When are eddy tracer fluxes directed downgradient? *Journal of Physical Oceanography, 36*(2), 189-201. doi:10.1175/jpo2841.1Youngs, M. K., Thompson, A. F., Lazar, A., & Richards, K. J. (2017). ACC Meanders, Energy Transfer, and Mixed Barotropic-Baroclinic Instability. *Journal of Physical Oceanography, 47*(6), 1291-1305. doi:10.1175/jpo-d-16-0160.1Zhao, R., & Vallis, G. (2008). Parameterizing mesoscale eddies with residual and Eulerian schemes, and a comparison with eddy-permitting models. *Ocean Modelling, 23*(1-2), 1-12. doi:10.1016/j.ocemod.2008.02.005

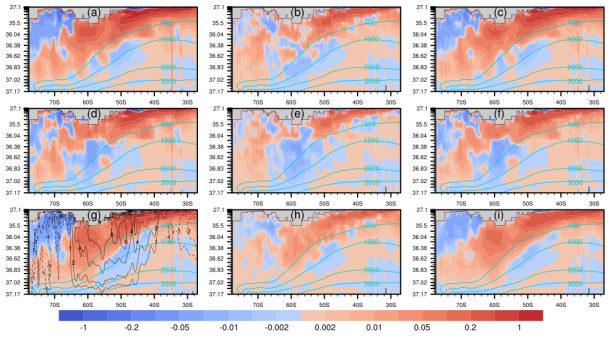

Figure 1 Zonal mean (a) total meridional PV transport (unit: $10^{-12}s^{-2}$), (b) total PV transport reconstruction by the isotropic transport coefficient, and (c) total PV transport reconstruction by the anisotropic transport tensor. (d)(e)(f) for the stationary component and (g)(h)(i) for the transient component. The green lines refer to the isopycnal depths (400 m, 1000 m, 2000 m, 3000 m), and the black in (g) refers to the zonal-averaged zonal velocity (unit: cm/s)

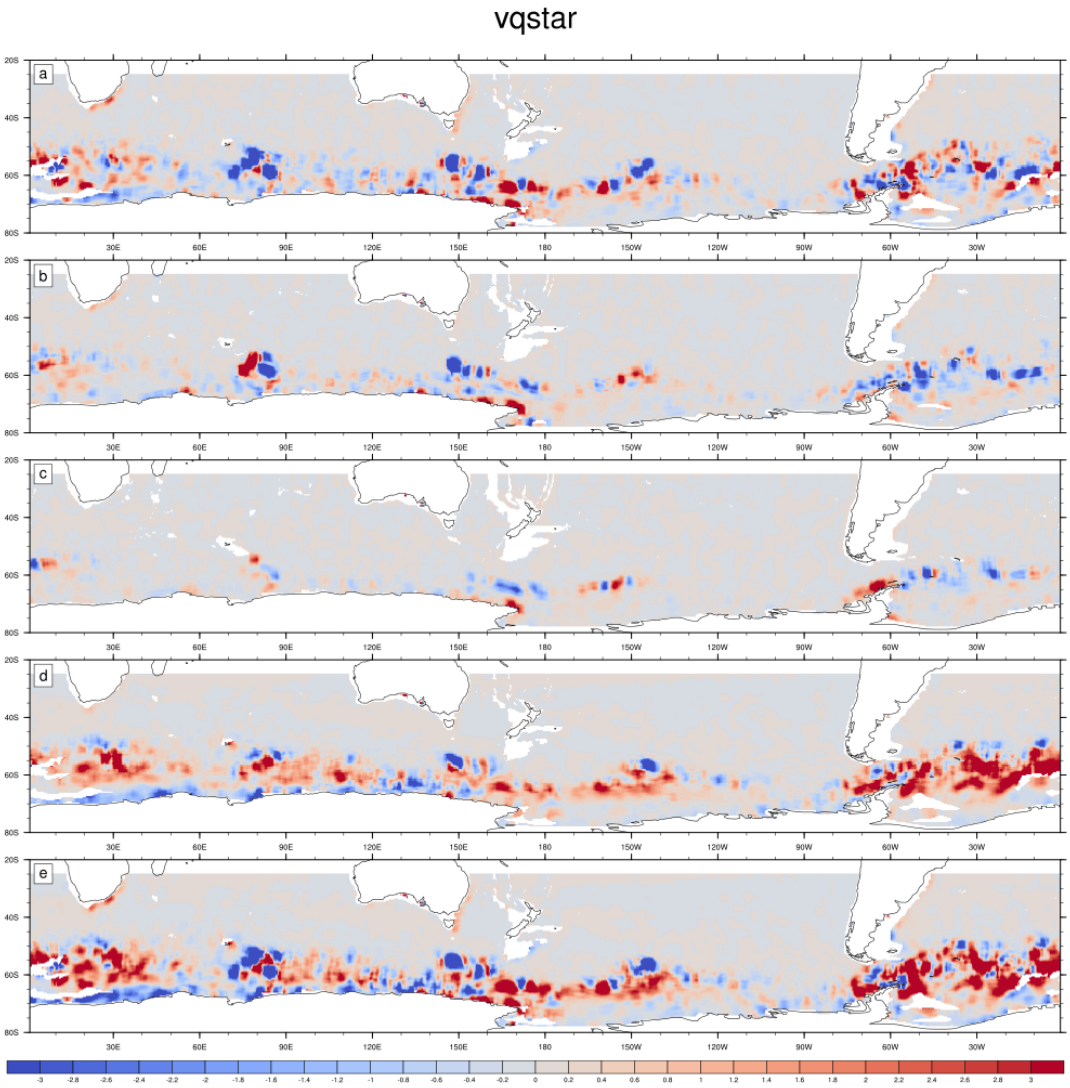

Figure 2 Meridional eddy PV transport (unit: $10^{-13}s^{-2}$), (a)(b)(c) for the stationary component on potential density surfaces $\ 2 = 36.38$, 36.62 and 36.83 kg/m^3, respectively, and (d) for the transient and (e) total transport on the surface of $\ 2 = 36.38$ kg/m^3

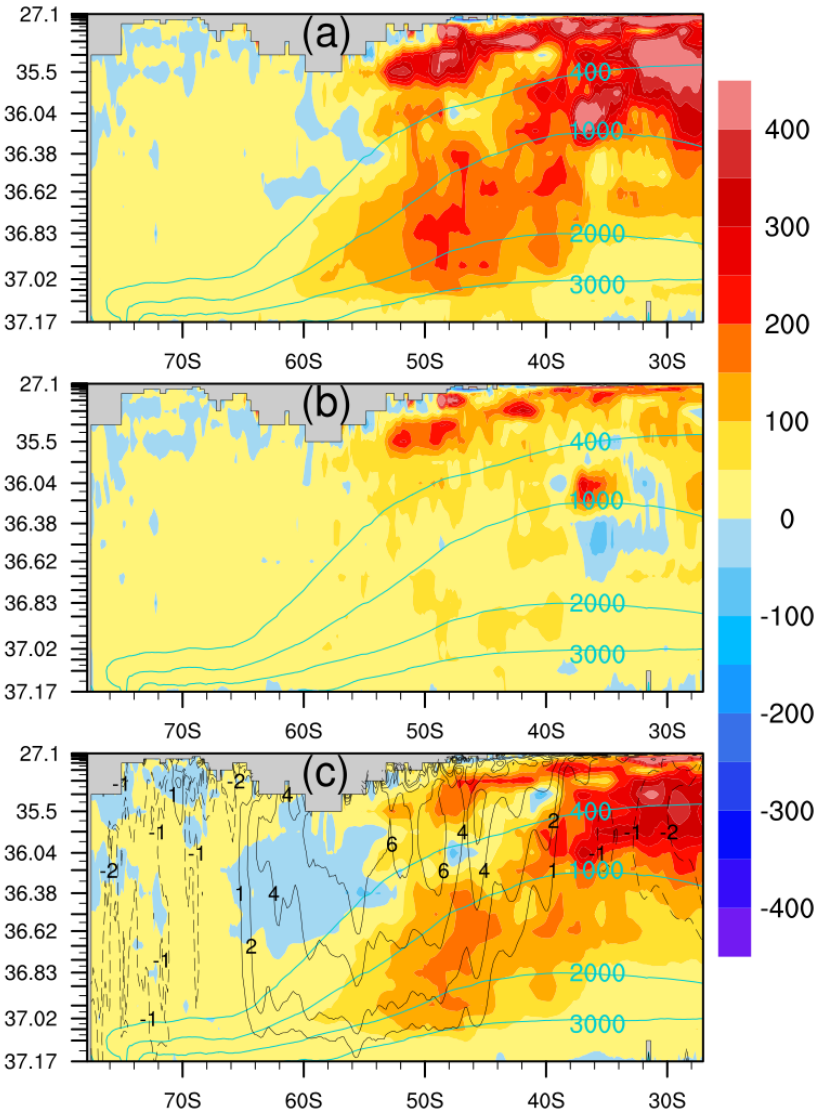

Figure 3 (a) Total, (b) stationary and (c) transient zonal mean isotropic transport coefficients (unit m^2/s)

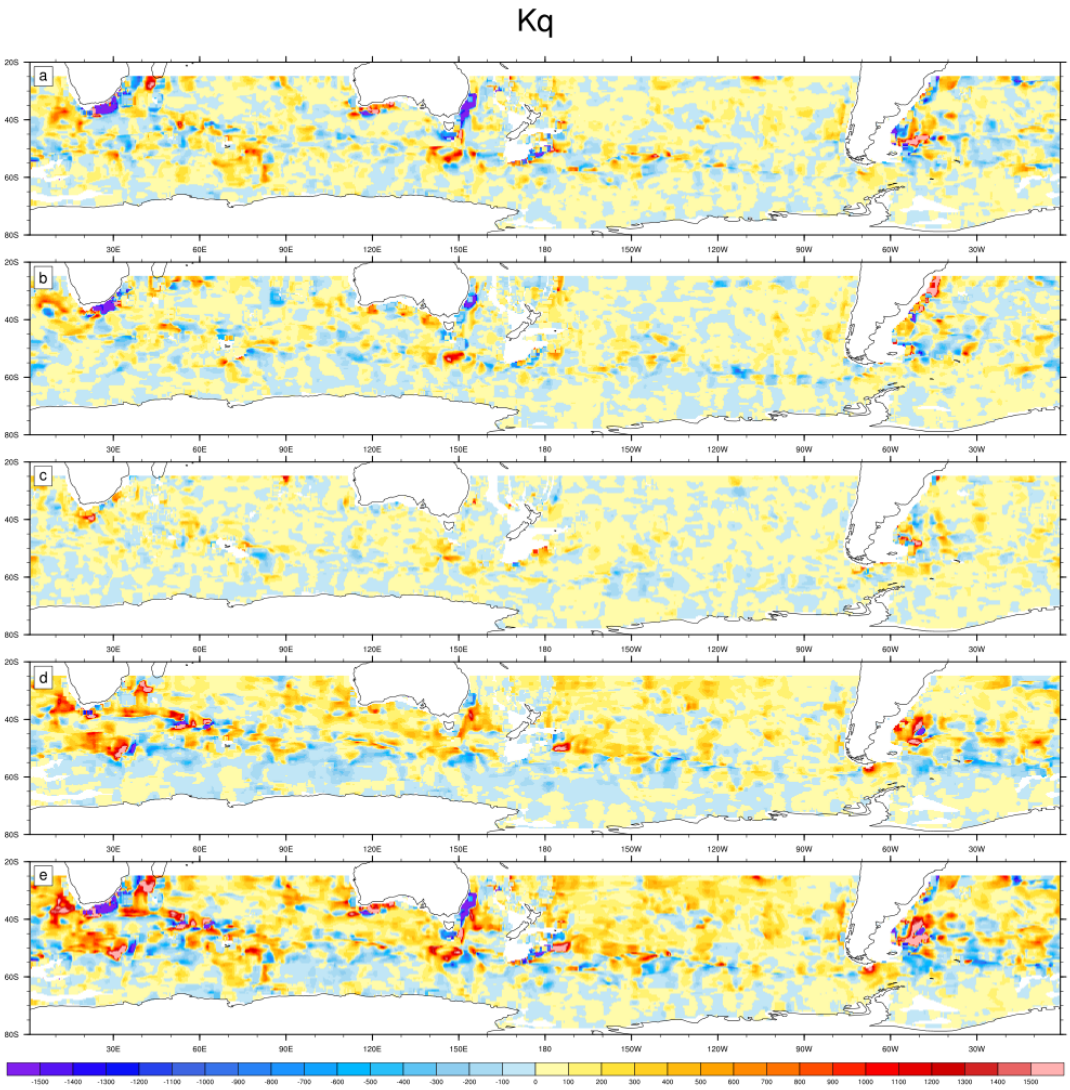

Figure 4 The isotropic transport coefficients (unit m^2/s), (a)(b)(c) for the stationary component on potential density surfaces $2 = 36.38$, 36.62 and 36.83 kg/m^3, respectively, and (d) for the transient and (e) total transport on the surface of $2 = 36.38$ kg/m^3

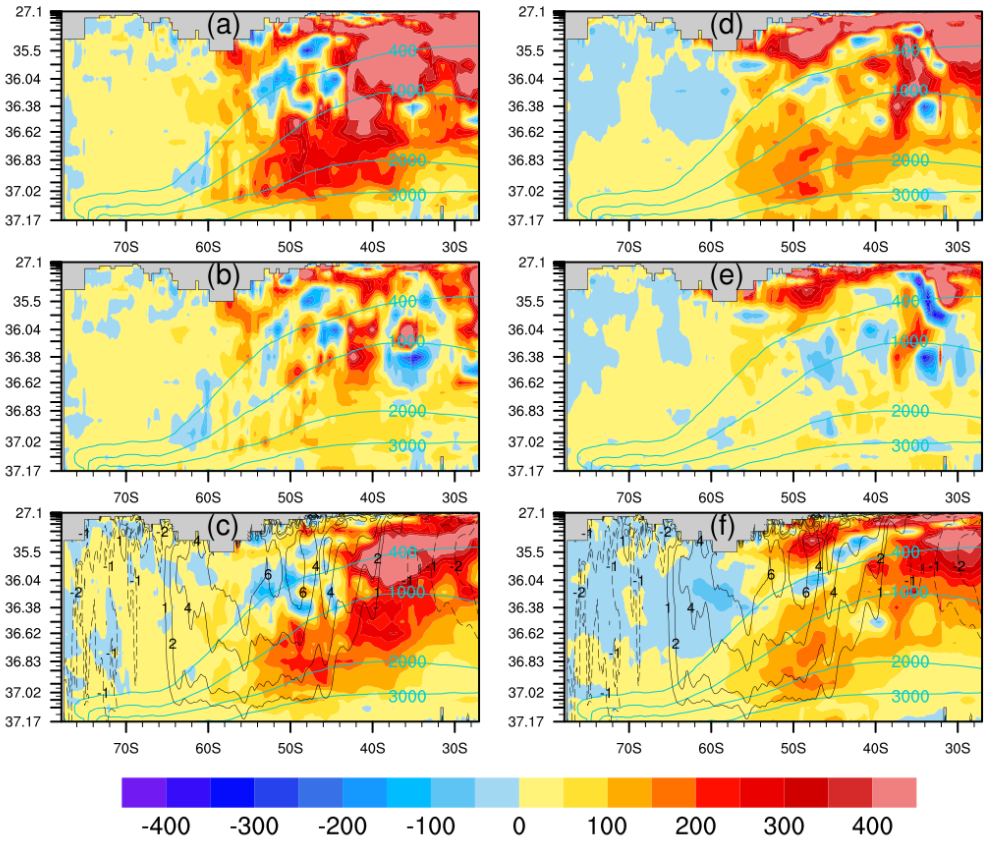

Figure 5 (a) Total, (b) stationary and (c) transient zonal mean anisotropic transport tensor elements Kxx (unit: m^2/s), (d)(e)(f) for those of Kyy in the same order

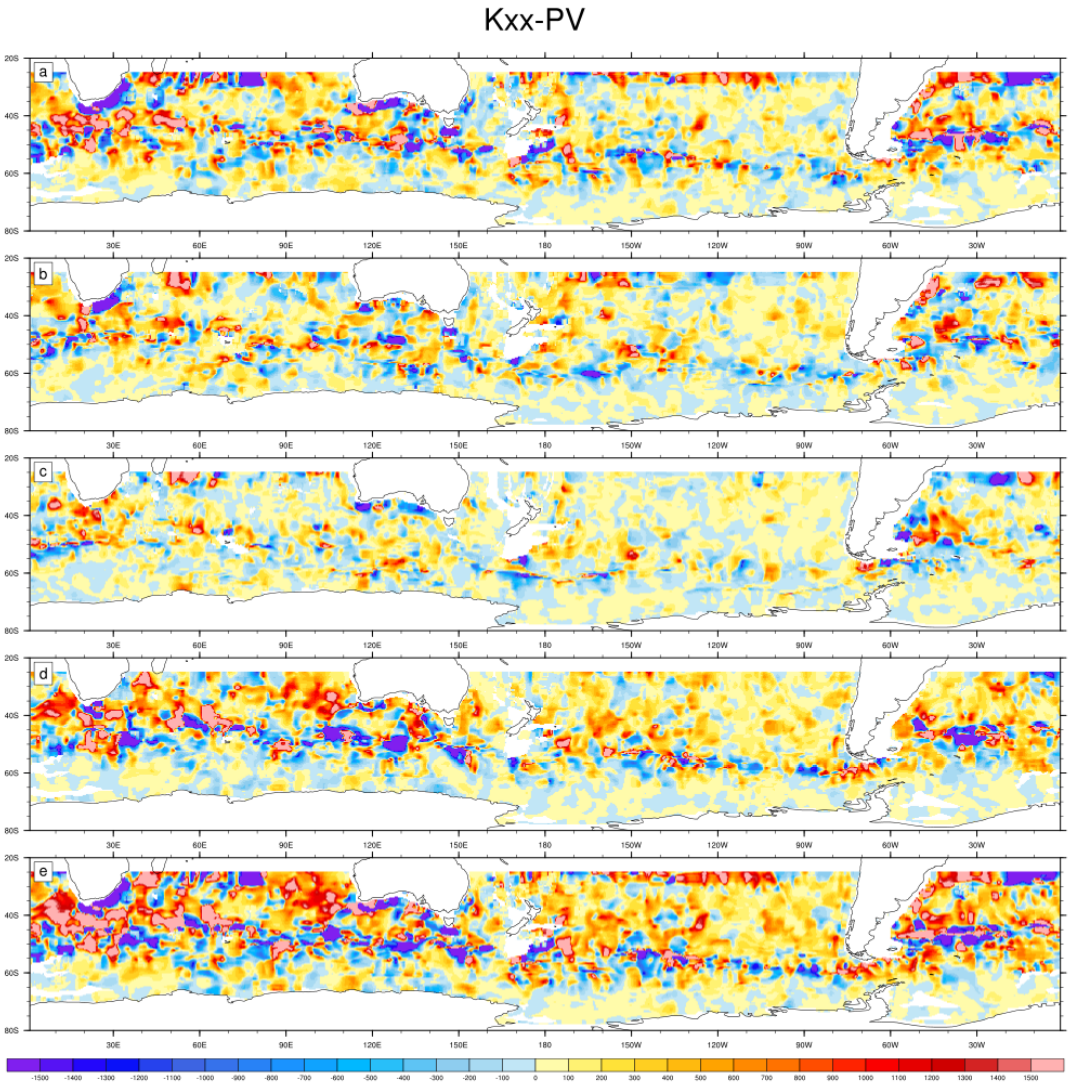

Figure 6 Same as Figure 4, but for the anisotropic transport tensor element Kxx

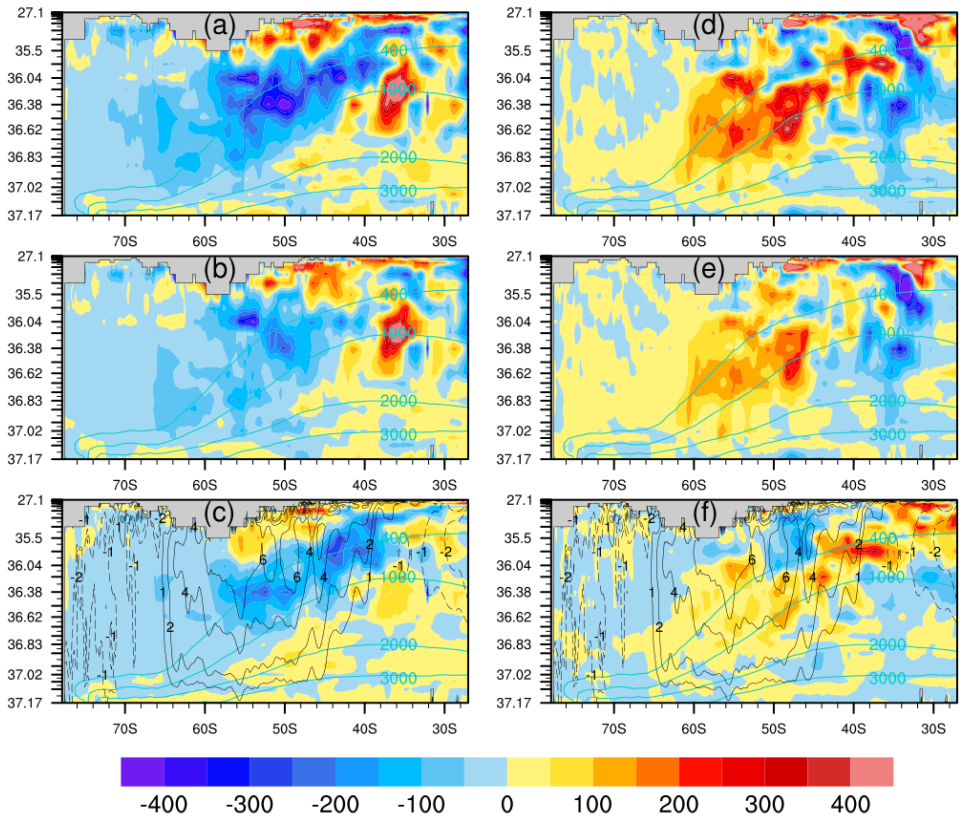

Figure 7 Same as Figure 5, but for Kxy (left column) and Kyx (right column)

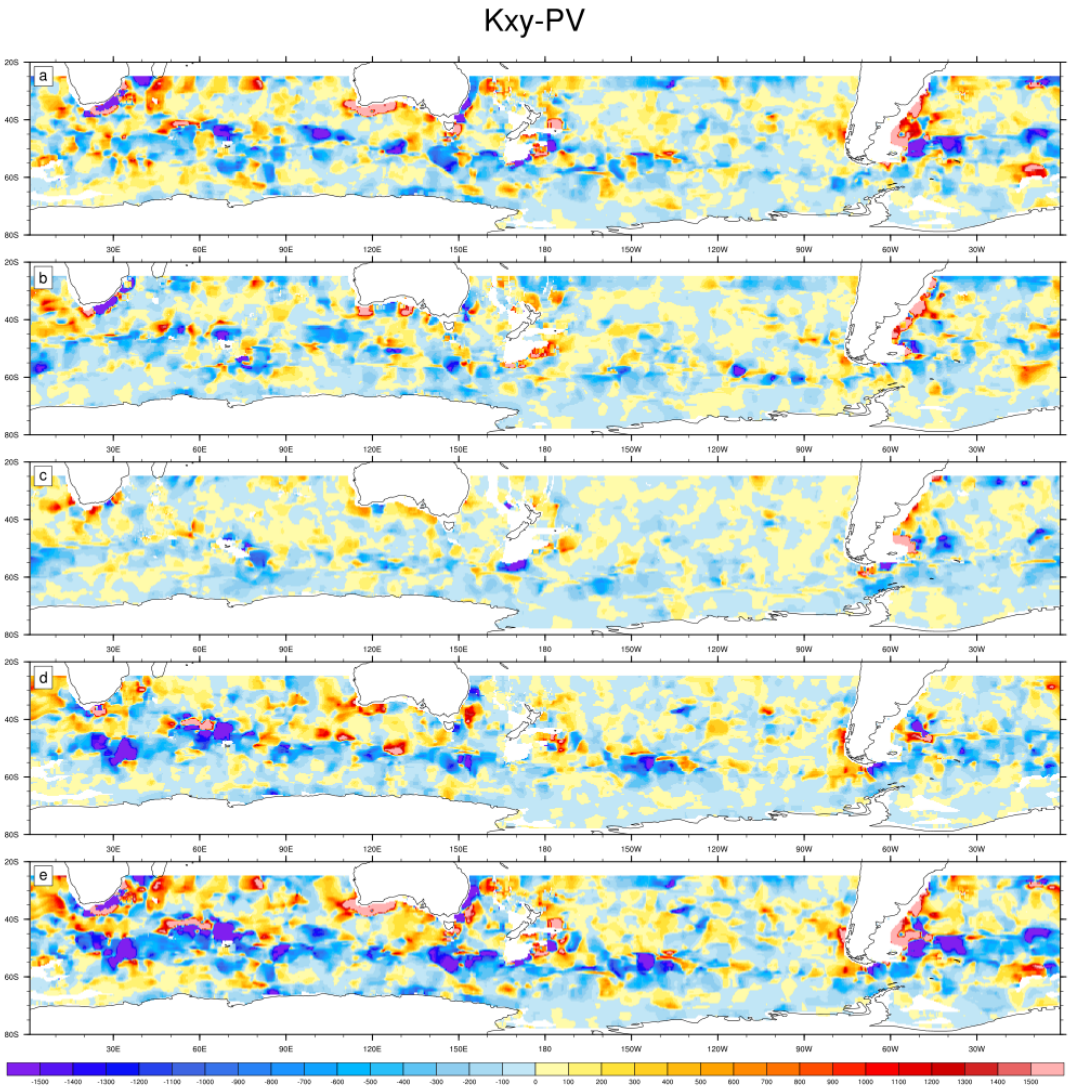

Figure 8 Same as Figure 4, but for the anisotropic transport tensor element Kxy

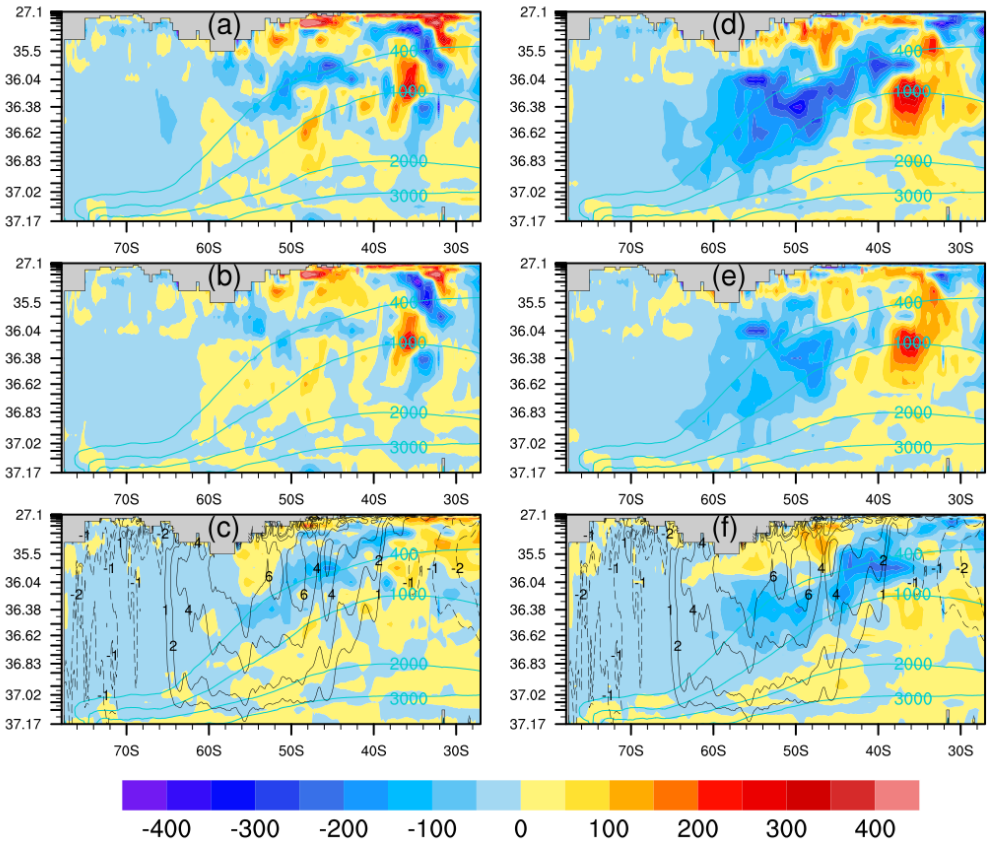

Figure 9 Same as Figure 5, but for Sxy (left column) and Ayx (right column)

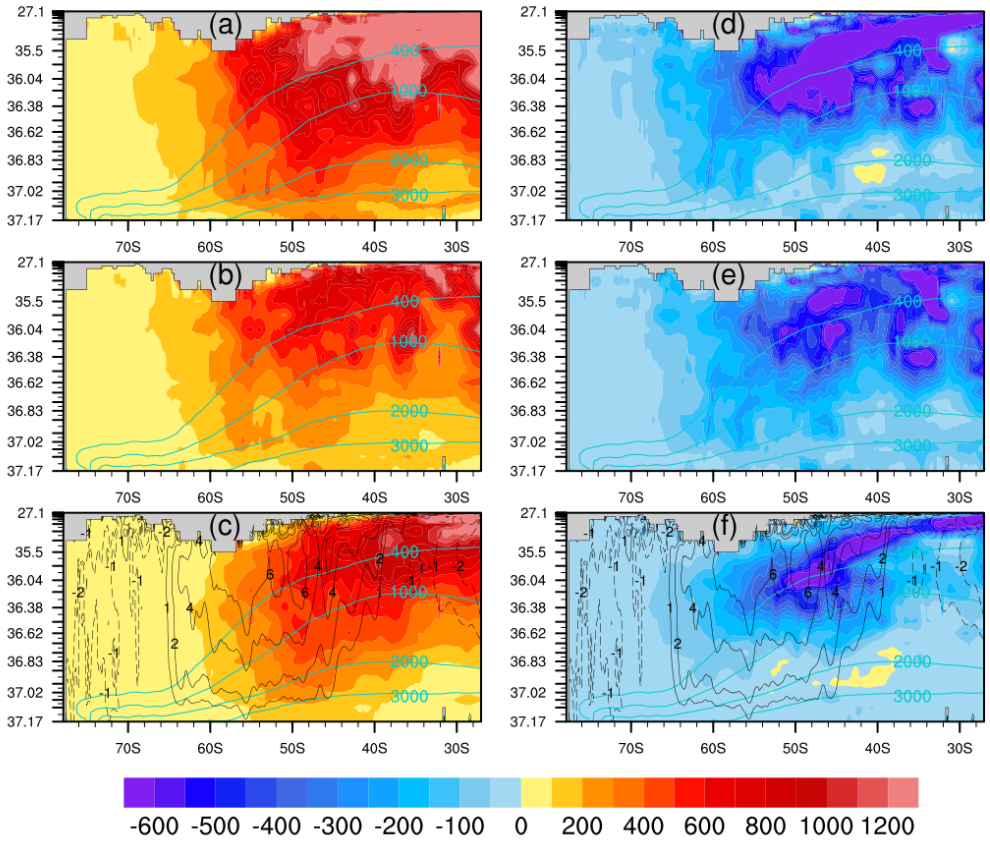

Figure 10 Same as Figure 5, but for the major eigenvalue (left column) and the minor eigenvalue (right column)

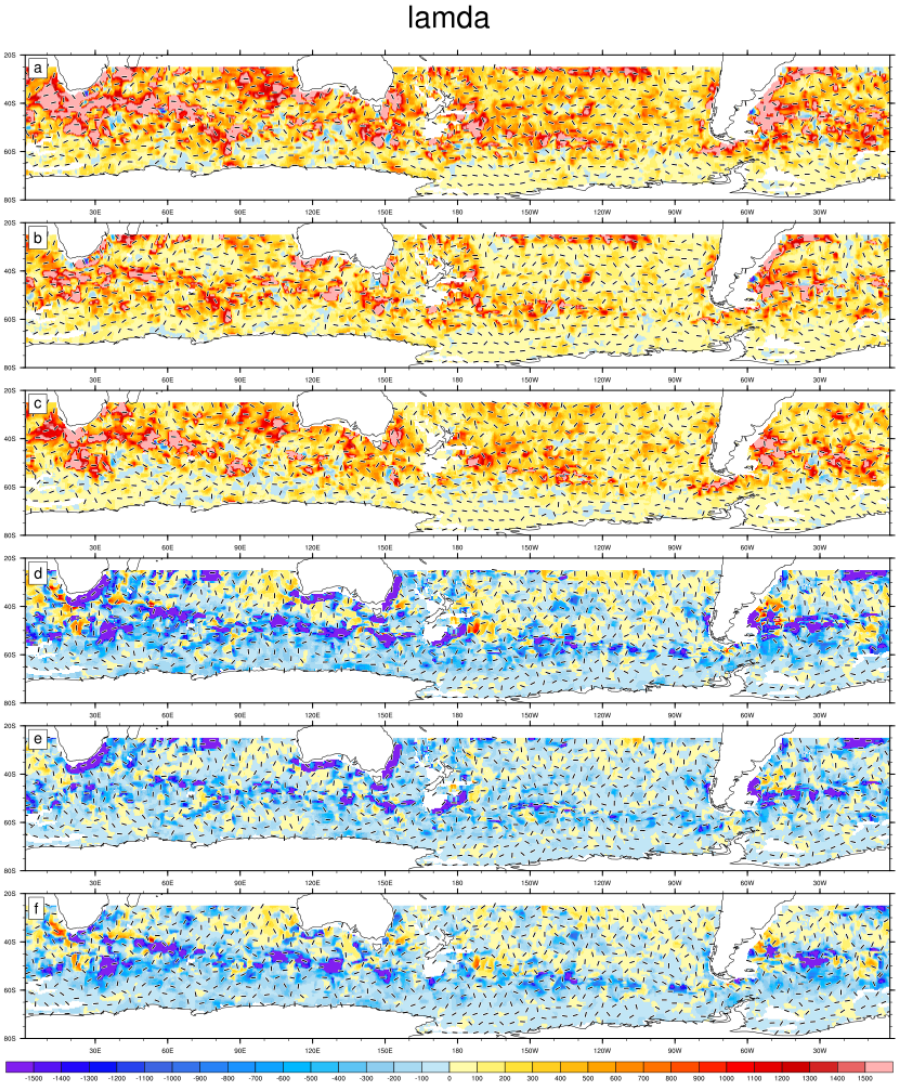

Figure 11 (a) Total, (b) stationary and (c) transient major eigenvalues on the isopycnal of $2 = 36.38\,\mathrm{kg/m^3}$, where (d)(e)(f) are those for the minor eigenvalues in the same order, and the black needle is the local characteristic direction

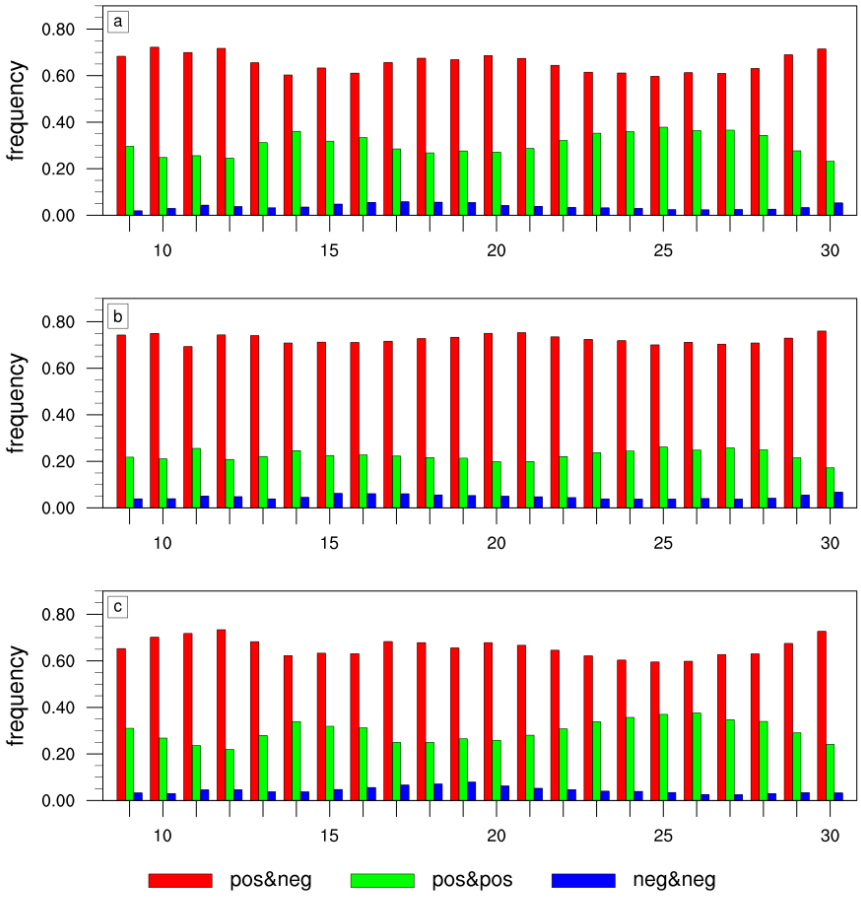

Figure 12 The frequency of the three eigenvalue configurations on each potential density surface, (a)(b)(c) for the total, stationary and transient cases, respectively. The results for layer 9 (2 = 32.6 kg/m^3) through layer 30 (2 = 37.17 kg/m^3) with enough valid points are shown

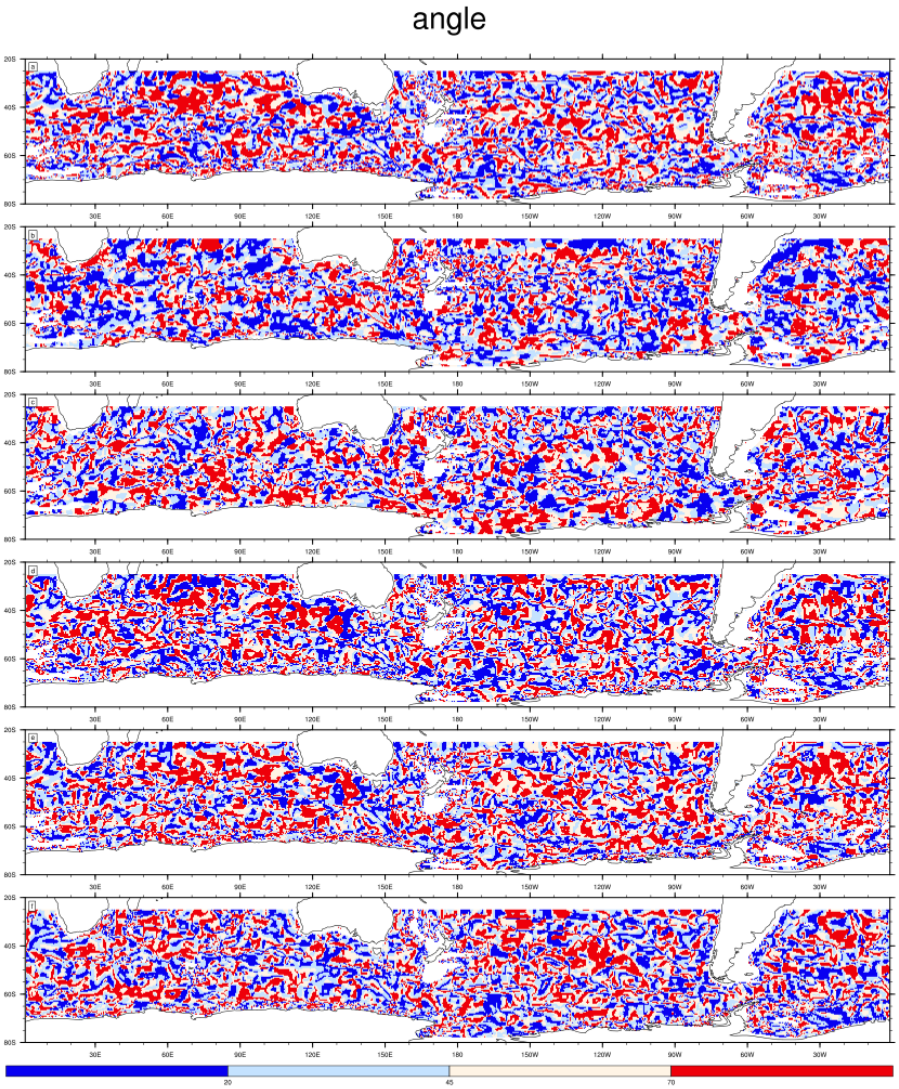

Figure 13 Absolute included angle between the total major eigenvector and the large-scale (a) PV gradient, (b) velocity vector and (c) topographic slope vector on the isopycnal of 36.38 kg/m^3. (d)(e) the angles between the large-scale PV gradient and the stationary or transient major eigenvector, respectively, on the isopycnal of 36.38 kg/m^3. (f) is the angle between the total major eigenvector and the large-scale PV gradient on the isopycnal of 36.62 kg/m^3

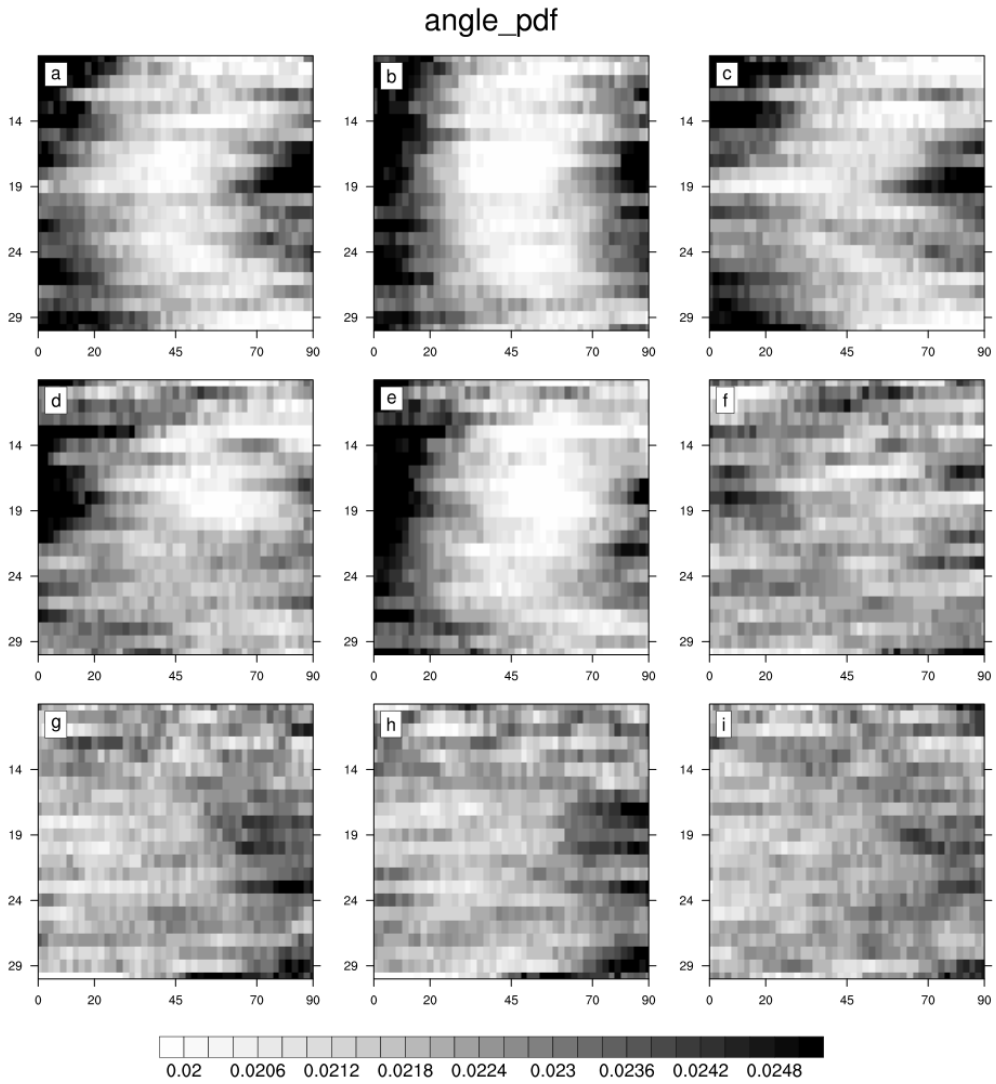

Figure 14 The probability density function and vertical structure of the absolute included angle between the (a) total, (b) stationary, and (c) transient major eigenvectors and the large-scale PV gradient. (d)(e)(f) and (g)(h)(i) are the same as (a)(b)(c), but for the results of the large-scale velocity vector and topographic slope vector, respectively. The x-axis is the angle, and the y axis is the label of the potential density layer. To ensure a sufficient number of samples, only layers 9 (2 = 32.6 kg/m^3) to 30 (2 = 37.17 kg/m^3) are displayed